

## Three-dimensional reacting shock–bubble interaction

Diegelmann, Felix; Hickel, Stefan; Adams, Nikolaus A.

**DOI**

[10.1016/j.combustflame.2017.03.026](https://doi.org/10.1016/j.combustflame.2017.03.026)

**Publication date**

2017

**Document Version**

Final published version

**Published in**

Combustion and Flame

**Citation (APA)**

Diegelmann, F., Hickel, S., & Adams, N. A. (2017). Three-dimensional reacting shock–bubble interaction. *Combustion and Flame*, 181, 1339-1351. <https://doi.org/10.1016/j.combustflame.2017.03.026>

**Important note**

To cite this publication, please use the final published version (if applicable). Please check the document version above.

**Copyright**

Other than for strictly personal use, it is not permitted to download, forward or distribute the text or part of it, without the consent of the author(s) and/or copyright holder(s), unless the work is under an open content license such as Creative Commons.

**Takedown policy**

Please contact us and provide details if you believe this document breaches copyrights. We will remove access to the work immediately and investigate your claim.



# Three-dimensional reacting shock–bubble interaction



Felix Diegelmann<sup>a,\*</sup>, Stefan Hickel<sup>a,b</sup>, Nikolaus A. Adams<sup>a</sup>

<sup>a</sup> Institute of Aerodynamics and Fluid Mechanics, Technische Universität München, Garching 85748, Germany

<sup>b</sup> Faculty of Aerospace Engineering, TU Delft, Delft 2629 HS, Netherlands

## ARTICLE INFO

### Article history:

Received 29 December 2016

Revised 8 March 2017

Accepted 27 March 2017

Available online 22 April 2017

### Keywords:

Shock-bubble interaction

Shock-induced ignition

Shock wave

Detonation

Shock-induced mixing

Richtmyer–Meshkov instability

## ABSTRACT

We investigate a reacting shock–bubble interaction through three-dimensional numerical simulations with detailed chemistry. The convex shape of the bubble focuses the shock and generates regions of high pressure and temperature, which are sufficient to ignite the diluted stoichiometric  $H_2$ – $O_2$  gas mixture inside the bubble. We study the interaction between hydrodynamic instabilities and shock-induced reaction waves at a shock Mach number of  $Ma = 2.83$ . The chosen shock strength ignites the gas mixture before the shock-focusing point, followed by a detonation wave, which propagates through the entire bubble gas. The reaction wave has a significant influence on the spatial and temporal evolution of the bubble. The misalignment of density and pressure gradients at the bubble interface, caused by the initial shock wave and the subsequent detonation wave, induces Richtmyer–Meshkov and Kelvin–Helmholtz instabilities. The growth of the instabilities is highly affected by the reaction wave, which significantly reduces mixing compared to an inert shock–bubble interaction. A comparison with two-dimensional simulations reveals the influence of three-dimensional effects on the bubble evolution, especially during the late stages. The numerical results reproduce experimental data in terms of ignition delay time, reaction wave speed and spatial expansion rate of the bubble gas. We observe only a slight divergence of the spatial expansion in the long-term evolution.

© 2017 The Authors. Published by Elsevier Inc. on behalf of The Combustion Institute.  
This is an open access article under the CC BY-NC-ND license.  
(<http://creativecommons.org/licenses/by-nc-nd/4.0/>)

## 1. Introduction

The interaction between a shock wave and a density inhomogeneity induces Richtmyer–Meshkov instability (RMI). The baroclinic vorticity production mechanism and subsequent Kelvin–Helmholtz instabilities (KHI) result in a complex turbulent flow field. The shock–bubble interaction (SBI) is a common setup to study this interaction, which has been done intensively for several decades [1]. An additional degree of complexity can be added by replacing the inert bubble gas by a reactive gas mixture. In the generic configuration of a reacting shock–bubble interaction (RSBI), the increase of pressure and temperature across the shock wave accelerates the chemical reactions. Depending on the shock strength, the stimulation of the reaction kinetics can be sufficient to ignite the reactive bubble gas. The subsequent reaction wave interacts with the hydrodynamic instabilities and affects integral properties of the flow field. By three-dimensional numerical simulation we investigate RSBI of a gas bubble filled with hydrogen ( $H_2$ ) and oxygen ( $O_2$ ), diluted with xenon (Xe) in a pure nitrogen ( $N_2$ ) environment at a shock Mach number of  $Ma = 2.83$ . The setup is

motivated by previous works of the authors [2,3], where the ignition behavior and the early stage bubble evolution of RSBI in two dimensions was investigated. Specific reaction wave types and ignition spots were triggered by the variation of the initial pressure or the shock strength. The subsequent mixing processes and the bubble evolution, including the spatial expansion and the growth of instabilities, showed a high dependence on the reaction wave type. Three-dimensional effects, which are relevant for the long-term evolution are the focus of the current work.

Shock-accelerated flows in reactive environments involve a wide range of scales, from extremely large scales in astrophysics [4], intermediate scales in combustion engines [5], down to very small scales in inertial confinement fusion [6]. Independent of the scale, the misalignment of the pressure gradient,  $\nabla p$ , associated with the shock wave, and the density gradient,  $\nabla \rho$ , across a material interface, produces baroclinic vorticity ( $\nabla p \times \nabla \rho$ ) and induces Richtmyer–Meshkov instability (RMI) [7,8], the impulsive limit of the Rayleigh–Taylor instability [9,10]. The RMI promotes turbulent mixing and increases the burning efficiency [11,12]. For a comprehensive review on RMI, the reader is referred to Brouillette [13]. Furthermore, the instability induces velocity shear and small perturbations at the interface of the bubble, which are, besides the initial density mismatch, necessary preconditions for the

\* Corresponding author.

E-mail address: [felix.diegelmann@aer.mw.tum.de](mailto:felix.diegelmann@aer.mw.tum.de) (F. Diegelmann).

Kelvin–Helmholtz instability (KHI) [14]. The perturbations are amplified and generate vortices at the interface accompanied by the appearance of smaller scales [13]. The breakup of large-scale structures is driven by the KHI [15,16] and forces mixing.

### 1.1. Shock–bubble interaction

The classical inert shock–bubble interaction (ISBI) describes the hydrodynamic effects induced by a planar shock wave propagating through a gas bubble. Upon contact, the incident shock wave is partially reflected and partially transmitted. For an Atwood number  $A = (\rho_1 - \rho_2)/(\rho_1 + \rho_2) < 0$  (the bubble gas is lighter than the ambient gas), the transmitted shock wave propagates faster than the incident shock wave.  $A > 0$  shows the converse effect: the transmitted shock wave travels slower than the incident shock wave outside the bubble. The transmitted shock wave focuses at the downstream pole of the bubble and collapses into a single shock-focusing point. RMI, due to the misalignment of the pressure and density gradient at the bubble interface, causes the bubble to evolve into a vortex ring. Provided that the initial kinetic-energy input is sufficient, the flow develops a turbulent mixing zone through non-linear interactions of the material interface perturbations [13,17].

ISBI was intensively studied over the last decades. The first detailed experimental investigations were performed by Haas and Sturtevant [18] in 1987. They studied gas bubbles filled with either helium or chlorodifluoromethane (R22), surrounded by air, and contributed with their results to a better understanding of the temporal bubble evolution under shock acceleration and established a new class of canonical flow configurations. Quirk and Karni [19] complemented these experimental findings by their detailed numerical results of shock–bubble interaction problems. Shock wave focusing, formation of a jet towards the center of the bubble and the transition from regular to irregular refraction were reproduced. For a detailed review of ISBI the reader is referred to Ranjan et al. [1].

### 1.2. Reacting shock–bubble interaction

The classical setup of ISBI can be extended replacing the inert bubble gas by a reactive gas mixture. Thus, the compression and temperature increase across the shock wave induce an additional effect: the chemical reaction rates are elevated, radicals form and accumulate. For sufficiently strong shock waves, the mixture ignites and reaction waves propagate through the reactive bubble gas.

Two reaction wave types have to be distinguished: deflagration and detonation. Deflagration is a subsonic diffusion-driven reaction wave that propagates through the gas mixture due to the direct transfer of thermal energy from burning to unburned gas [20]. Detonation is driven by a fast chemical reaction and the associated large heat release within the reaction wave. A shock wave immediately precedes the detonation wave and preheats the gas mixture by compression [20]. Detonation waves propagate up to  $10^8$  times faster than deflagration waves [21]. The latter reaction wave is observed and studied in our numerical investigation of RSBI.

First experimental studies of RSBI were performed by Haehn et al. [22] in 2012. In their setup, a gas bubble filled with a stoichiometric mixture of  $H_2$  and  $O_2$ , diluted by xenon (Xe) is penetrated by a shock wave with shock Mach numbers between  $Ma = 1.34$  and  $Ma = 2.83$ . A weak shock wave with  $Ma = 1.34$  does not ignite the gas mixture within the experimental timeframe. Compression is not sufficient to start a self-sustaining chemical reaction. An increase of the shock strength results in ignition, followed by a deflagration wave. The reaction wave type changes for higher shock Mach numbers; Haehn et al. [22] observed a detonation wave for  $Ma = 2.83$ , even before the shock wave has reached

the shock focusing point. They conclude, that the post-shock thermodynamic conditions are near the ignition limits. Several chemiluminescence exposures are provided by Haehn et al. [22] to depict the qualitative evolution of the bubble and the reaction processes. The reaction wave has propagated through the bubble gas before the formation of the vortex ring is initiated. Furthermore quantitative data for the temporal evolution of the transverse diameter of the bubble as well as for the vortex ring diameter are presented. However, the complex experimental setup implies uncertainties. Haehn et al. [22] estimate the uncertainty of the Damköhler number at the highest shock Mach number ( $Ma = 2.83$ ) of up to 50% ( $Da = 8 \pm 4$ ). At the lowest shock Mach number ( $Ma = 1.34$ ) 30% of all measurements showed no ignition within the given experimental time frame. Numerical studies are necessary to obtain a deeper understanding of the physics and reaction kinetics of RSBI. Accurate numerical simulations can provide detailed insight into induction times, gas compositions and mixing processes during the shock–bubble interaction.

We presented first numerical results for two-dimensional RSBI [2,3]. Pressure dependent ignition and reaction waves were in agreement with experiments of Haehn et al. [22]. Despite the missing spatial dimension, the simulations reproduced bubble expansion, ignition location and reaction wave types, and explained experimentally particularities, such as the transition from deflagration to detonation and a double detonation. Nevertheless, some important effects, especially for the long-term evolution, were suppressed as the vortex stretching term is absent in two dimensions. The two-dimensional vortex cores remain stable, whereas three-dimensional vortex rings become unstable and may break up into three-dimensional turbulence [23]. In order to obtain accurate predictions for the mixing processes in the long-term evolution of RSBI, an extension to three-dimensional simulations is needed.

### 1.3. Scope of the present work

The present numerical investigation extends our previous work on two-dimensional RSBI [2,3] and complements the experimental results of Haehn et al. [22] by three-dimensional RSBI simulations with detailed  $H_2$ – $O_2$  chemistry. At a shock Mach number of  $Ma = 2.83$  the mixture ignites ahead of the shock-focusing point. Ignition is followed by a detonation wave that has a distinct effect on the hydrodynamic evolution of the RSBI. We also present results for ISBI to study the influence of the reaction wave on the mixing process, on the vortex ring and on the spatial and temporal bubble evolution. By comparison with two-dimensional simulations, we are able to show how three-dimensional phenomena, such as the decaying vortex ring, destabilized by Widnall-type instabilities, influence the long-term evolution of SBI. The experimental findings of Haehn et al. [22] are confirmed and important quantities such as the ignition delay time, the reaction wave speed, and the spatial and temporal bubble evolution are correctly reproduced.

This paper is structured as follows: Section 2 summarizes the governing equations for fluid dynamics and chemical reaction kinetics. Initial conditions and the computational domain are presented in Section 3. Section 4.1 outlines the results of the three-dimensional simulations, followed by a comparison with two-dimensional data in Section 4.2. In Section 4.3, we compare our results with the experimental work of Haehn et al. [22]. The final Section 5 summarizes the key findings.

## 2. Numerical model

### 2.1. Governing equations

We solve the full set of compressible reacting multi-component Navier–Stokes equations in conservative form

$$\frac{\partial \mathbf{U}}{\partial t} + \nabla \cdot \mathbf{F}(\mathbf{U}) = \nabla \cdot \mathbf{F}_v(\mathbf{U}) + \mathbf{S}, \quad (1)$$

with

$$\mathbf{U} = \begin{pmatrix} \rho \\ \rho \mathbf{u} \\ E \\ \rho Y_i \end{pmatrix}, \quad \mathbf{F}(\mathbf{U}) = \begin{pmatrix} \rho \mathbf{u} \\ \rho \mathbf{u} \mathbf{u} + p \boldsymbol{\delta} \\ (E + p) \mathbf{u} \\ \rho \mathbf{u} Y_i \end{pmatrix}, \quad (2)$$

$$\mathbf{F}_v(\mathbf{U}) = \begin{pmatrix} 0 \\ \boldsymbol{\tau} \\ \boldsymbol{\tau} \cdot \mathbf{u} - \mathbf{q}_c - \mathbf{q}_d \\ \mathbf{J}_i \end{pmatrix} \quad \text{and} \quad \mathbf{S} = \begin{pmatrix} 0 \\ \mathbf{0} \\ \dot{\omega}_T \\ \dot{\omega}_i \end{pmatrix}.$$

The solution vector  $\mathbf{U}$  consists of mass density  $\rho$ , momentum  $\rho \mathbf{u}$ , total energy  $E$  and the mass fractions  $Y_i$  of species  $i = 1, 2, \dots, N$ , with  $N$  being the total number of species. The identity matrix is given by  $\boldsymbol{\delta}$  and pressure by  $p$ .  $\mathbf{q}_c$  represents the heat conduction,  $\mathbf{q}_d$  the interspecies diffusional heat flux and  $\mathbf{J}_i$  the species diffusion. The heat release  $\dot{\omega}_T$  and species formation and destruction in terms of individual mass rates  $\dot{\omega}_i$  represent the chemical reaction kinetics.

The viscous stress tensor  $\boldsymbol{\tau}$  for a Newtonian fluid is given by

$$\boldsymbol{\tau} = 2\bar{\mu} \left[ \frac{1}{2} (\nabla \mathbf{u} + (\nabla \mathbf{u})^T) - \frac{1}{3} \boldsymbol{\delta} (\nabla \cdot \mathbf{u}) \right], \quad (3)$$

with  $\bar{\mu}$  as the mixture viscosity. We define the heat conduction according to the Fourier law as

$$\mathbf{q}_c = -\bar{\kappa} \nabla T, \quad (4)$$

where  $\bar{\kappa}$  is the mixture heat conductivity. The interspecies diffusional heat flux  $\mathbf{q}_d$  [24] is defined as

$$\mathbf{q}_d = \sum_{i=1}^N h_i \mathbf{J}_i, \quad (5)$$

with  $h_i$  as the individual species enthalpy. The inclusion of interspecies diffusional heat flux is important to prevent anomalous temperature gradients and spurious pressure oscillations, especially in combustion processes [24]. The species diffusion  $\mathbf{J}_i$  is given by

$$\mathbf{J}_i = -\rho \left( D_i \nabla Y_i - Y_i \sum_{j=1}^N D_j \nabla Y_j \right). \quad (6)$$

$D_i$  describes the effective binary diffusion coefficient of species  $i$ . For a detailed description of the equations and methods used to calculate caloric and transport properties, the reader is referred to our previous papers [2,3].

We close the equations by the equation of state for an ideal gas

$$p = \rho \bar{R} T \quad (7)$$

and

$$p = (\bar{\gamma} - 1) E. \quad (8)$$

$\bar{\gamma}$  represents the ratio of specific heats of the mixture

$$\bar{\gamma} = \frac{\bar{c}_p}{\bar{c}_p - \bar{R}}, \quad (9)$$

with

$$\bar{c}_p = \sum_{i=1}^N Y_i c_{p,i}. \quad (10)$$

The specific gas constant of the mixture is defined by  $\bar{R} = R/\bar{M}$ , with  $R$  as the universal gas constant.  $\bar{M}$  is the molar mass of the mixture

$$\bar{M} = \left[ \sum_{i=1}^N \frac{Y_i}{M_i} \right]^{-1} = \sum_{i=1}^N X_i M_i, \quad (11)$$

where  $X_i$  is the mole fraction and  $M_i$  the molar mass of species  $i$ .  $c_{p,i}$  represents the specific heat coefficients at constant pressure.

## 2.2. Reaction kinetics

Chemical reaction kinetics are represented by the source term in Eq. (1), containing the heat release  $\dot{\omega}_T$  and species formation and destruction in terms of individual mass rates  $\dot{\omega}_i$ . The specific heat release  $\dot{\omega}_T$  is defined as

$$\dot{\omega}_T = - \sum_{i=1}^N \Delta h_{f,i}^0 \dot{\omega}_i, \quad (12)$$

where  $\Delta h_{f,i}^0$  is the heat of formation of each species  $i$ . The mass rates  $\dot{\omega}_i$  for each species are calculated by

$$\dot{\omega}_i = W_i \sum_{r=1}^{N_R} \nu_{ir} \Gamma_r \left( k_{fr} \prod_{i=1}^N [X_i]^{\nu'_{ir}} - k_{br} \prod_{i=1}^N [X_i]^{\nu''_{ir}} \right). \quad (13)$$

$N_R$  is the number of reactions,  $W_i$  the molecular weight,  $\Gamma_r$  the third body efficiency of reaction  $r$ ,  $X_i$  the molar concentration, and  $\nu'_{ir}$  and  $\nu''_{ir}$  the molar stoichiometric coefficients of the reactant and the product of reaction  $r$ . The net stoichiometric coefficient  $\nu_{ir}$  is calculated by

$$\nu_{ir} = \nu''_{ir} - \nu'_{ir}. \quad (14)$$

The forward and backward reaction rates  $k_{fr}$  and  $k_{br}$  are calculated by the Arrhenius law,

$$k_{fr} = A_{fr} T^{\beta_{fr}} \exp\left(\frac{E_{fr}}{RT}\right). \quad (15)$$

$A_{fr}$  is the pre-exponential factor,  $E_{fr}$  is the activation energy and  $\beta_{fr}$  is the temperature exponent for each reaction  $r$  [25]. The equilibrium constants  $K_{cr}$  is used to estimate the backward reaction rates

$$k_{br} = \frac{k_{fr}}{K_{cr}}. \quad (16)$$

We calculate the equilibrium  $K_{cr}$  from

$$K_{cr} = \left(\frac{p^\circ}{RT}\right)^{\nu_r} \exp\left(\frac{\Delta S_{r,i}^\circ}{R} - \frac{\Delta H_{r,i}^\circ}{RT}\right), \quad (17)$$

where  $p^\circ$  is a pressure of 1 atm,  $\nu_r$  the net change in the number of species in the reaction,  $\Delta S_{r,i}^\circ$  the net change in entropy and  $\Delta H_{r,i}^\circ$  the net change in enthalpy.

Specific intermediate reactions have to be treated as duplicated reactions, by extending Eq. (15) to

$$k_{fr} = \sum_{i=1}^2 A_{fr_i} T^{\beta_{fr_i}} \exp\left(\frac{E_{fr_i}}{RT}\right). \quad (18)$$

One reaction consists of two sets of Arrhenius rate parameters, which lead to two forward reaction rates. The sum of both reactions result in the forward reaction rates  $k_{fr}$  of reaction  $r$ .

Furthermore, pressure dependence of specific intermediate reactions is considered by the calculation of two forward reaction rates for one reaction.  $k_{fr_0}$  for the high-pressure and  $k_{fr_\infty}$  for the low-pressure limit. A blending function composed of these high- and low-pressure Arrhenius rate parameters is applied for a smooth pressure dependence. For more details on the so-called fall-off reactions the reader is referred to Troe [26].

The accuracy of the reaction kinetics depends on the choice of the reaction mechanism, which provides the parameters of the

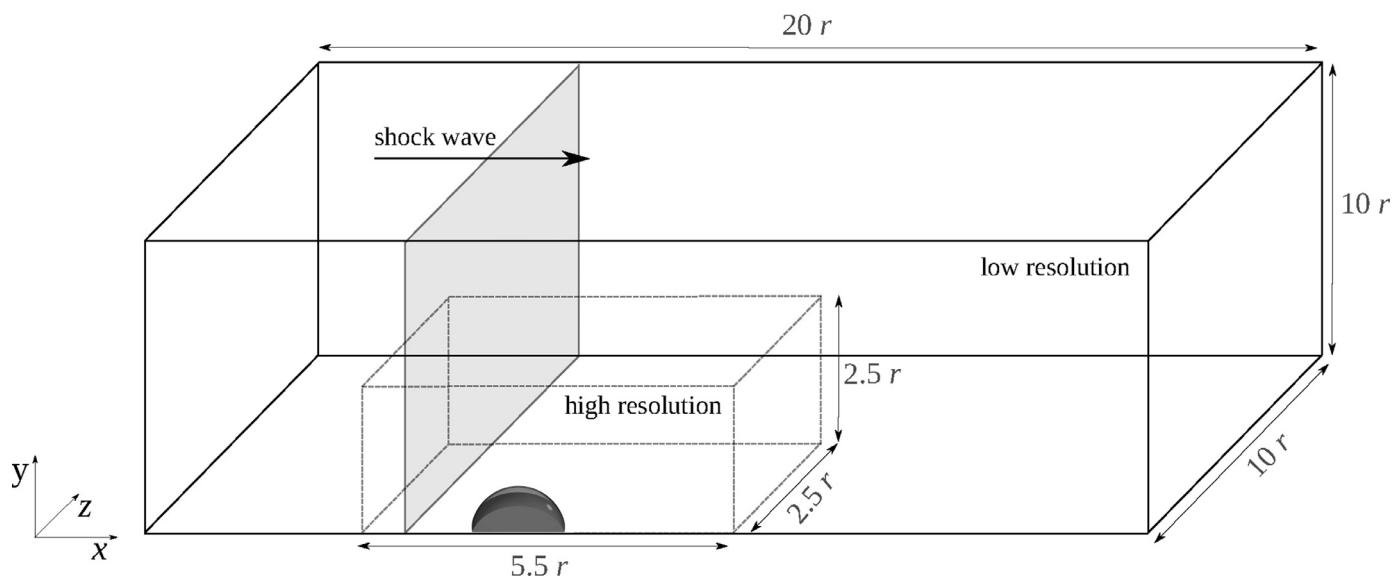


Fig. 1. Schematic of the computational domain with quarter-spherical bubble, filled with  $H_2$ ,  $O_2$  and Xe, surrounded by pure  $N_2$ .

Arrhenius law. Available mechanisms show large discrepancies in the number of reactions and species and in the consideration of third body efficiencies, duplicated and pressure dependent reactions. In RSBI, a setup which exhibits a wide pressure and temperature range, accurate results can only be achieved with a precise prediction of the ignition delay time. Therefore, utilization of a complex mechanism is inevitable, third body efficiencies, duplicated and pressure dependent reactions have to be considered. In a previous study [2], the necessity for a complex mechanism was shown. Simpler mechanisms were not able to predict the correct ignition delay time with a deviation of up to several magnitudes.

The Ó Conaire [27] reaction mechanism is applied in the presented work. The mechanism is validated for temperatures between 298 and 2700 K and a pressure range from 0.05 to 87 atm. Eight species participate in the reaction of  $H_2$  and  $O_2$  (two reactants:  $H_2$ ,  $O_2$ ; 5 chain-carrying intermediates: hydrogen radical (H), oxygen radical (O), hydroxyl radical (OH), hydroperoxyl radical ( $HO_2$ ), hydrogen peroxide ( $H_2O_2$ ); the product: hydrogen oxide ( $H_2O$ ) and 19 intermediate reactions are considered, including duplicated and pressure dependent reactions as well as third-body efficiencies. The two-body recombination reaction is stabilized by the absorption of energy by the third-bodies. The third-body efficiencies of Xe are set as the same as for argon (Ar), which are given by Ó Conaire [27]. The available modes, controlling the energy absorption, of Ar and Xe are identical, hence the third-body efficiencies can be assumed to be comparable. Also the steric factor for monoatomic gases, accounting for the geometry influence on the collision between molecules, is similar [28].

### 2.3. Numerical method

We apply the 2nd-order accurate Strang time splitting scheme [29] to solve the compressible reacting multi-component Navier–Stokes equations (Eq. (1)). The splitting scheme separates the stiff terms, containing the chemical reaction kinetics ( $\dot{\omega}_r$  and  $\dot{\omega}_i$ ), from the Navier–Stokes equations. The resulting system of partial differential equations (PDE) and the stiff system of ordinary differential equations (ODE) is solved separately. The PDE system is solved by the 3rd-order Runge–Kutta time-marching scheme of Gottlieb and Shu [30] with a finite-volume discretization scheme that applies a flux projection onto local characteristics for the hyperbolic part. The Roe matrix required for the projection is calculated for the full multi-species system [31,32]. The

numerical fluxes at the cell faces are reconstructed from cell averages by a central-upwind 6th-order weighted essentially non-oscillatory (WENO-CU6) scheme [33]. The scheme uses a non-dissipative 6th-order central stencil in smooth flow regions and a non-linear convex combination of 3rd-order stencils in regions with steep gradients. The characteristic flux reconstruction with general multi-component Roe-average [34] has been found necessary to avoid spurious pressure and temperature oscillations at material interfaces, which are a common problem in multi-species flows at material interfaces in general [35] and in the interaction between material interfaces and shock waves [36]. Previous studies have proven the capability for shock induced turbulent multi-species mixing problems of our scheme at finite Reynolds numbers [15,16,37,38] and for shock–bubble interactions including complex chemistry [2,3]. The stiff ODE system, containing the specific heat release and mass rates for each species is solved by a variable-coefficient ODE solver using 5th-order backward differentiation formulae [39].

## 3. Computational setup

### 3.1. Computational domain

RSBI is studied on a Cartesian grid in a three-dimensional domain with a quarter-spherical bubble, shown in Fig. 1. We impose inflow boundary conditions at the left domain boundary and outflow boundary conditions at the right, rear and upper domain boundaries. Symmetry boundary conditions are applied at the two cut surfaces of the bubble. The domain size is set to  $20r \times 10r \times 10r$ , with  $r$  as the initial bubble radius. The distance to the boundaries is chosen sufficiently large to avoid artifacts due to shock reflections. Grid resolution is increased around the bubble, regions outside of this area have a coarser resolution to reduce computational costs. The simulations are performed at a resolution of 140 points per radius (ppr) in the fine region, which amounts to a total number of 115 million cells.

The gas bubble is placed in a pure nitrogen ( $N_2$ ) environment and contains a stoichiometric mixture of  $H_2$ ,  $O_2$  and Xe in a composition of 2 / 1 / 3.67 mole fractions. The heavy inert gas Xe increases the Atwood number to  $A = 0.476$ . The bubble radius is set to  $r = 0.02$  m. A sharp and fully resolved interface between the bubble gas and the surrounding is defined in terms of the molar

fraction of  $N_2$

$$X_{N_2} = \frac{\tanh((\sqrt{x^2 + y^2 + z^2} - r) \xi) + 1}{2}, \quad (19)$$

with  $r$  as the radius of the bubble and  $\xi$  as the parameter controlling steepness, which is set to  $\xi = 20.000 \text{ m}^{-1}$ . The molar fraction ( $X = 1 - X_{N_2}$ ) inside the bubble is distributed among the three gases, ensuring the stoichiometric mixture with a relative composition of 2 / 1 / 3.67 ( $H_2 / O_2 / Xe$ ).

The shock wave propagates from the left to the right and is initialized near the upstream pole of the bubble. The pre-shock state is defined by  $T_0 = 295 \text{ K}$  and  $p_0 = 1.0 \text{ atm}$ . The shock Mach number is set to  $Ma = 2.83$ . The post-shock thermodynamics state is defined by standard Rankine–Hugoniot conditions

$$\rho'_{N_2} = \rho_{N_2} \frac{(\gamma_{N_2} + 1) Ma^2}{2 + (\gamma_{N_2} - 1) Ma^2}, \quad (20)$$

$$u'_{N_2} = Ma c_{N_2} \left(1 - \frac{\rho_{N_2}}{\rho'_{N_2}}\right), \quad (21)$$

$$p'_{N_2} = p_0 \left(1 + 2 \frac{\gamma_{N_2}}{\gamma_{N_2} + 1} (Ma^2 - 1)\right), \quad (22)$$

with  $c_{N_2} = \sqrt{\gamma_{N_2} p_0 / \rho_{N_2}}$ , which defines the speed of sound in nitrogen. Variables indicating post-shock conditions are marked with a prime. Initial data are set as the nominal conditions of the experimental setup of Haehn et al. [22].

### 3.2. Convergence study

We have performed an extensive grid resolution study to establish that our simulation results are grid-converged in terms of quantities of interest. We define the resolution in points per radius (ppr) of the gas bubble. Previous studies of ISBI showed convergence between 100 and 134 ppr. Niederhaus et al. [40] simulated ISBI at 128 ppr and resolved the initial bubble interface with 2 cells. Further studies of Ranjan et al. [41] achieved a converged solution with 134 ppr at similar shock Mach numbers as applied in our investigation. Hejazialhosseini et al. [42] showed converged integral quantities at 100 ppr. Even at high shock Mach numbers of  $Ma = 10$ , a resolution of 120 ppr was sufficient to resolve the quantities of interest according to Nakamura et al. [43].

For our grid resolution study, we analyze the error of the molar mixing fraction  $\Theta$  (MMF) for the mixing between the inert bubble gas Xe and the surrounding gas  $N_2$ . MMF can be interpreted as the ratio of molecular mixing to large-scale entrainment by convective motion and is defined by Danckwerts [44] as

$$\Theta(t) = \frac{\int_{-\infty}^{\infty} \int_{-\infty}^{\infty} \langle X_{N_2} X_{Xe} \rangle dx dz}{\int_{-\infty}^{\infty} \int_{-\infty}^{\infty} \langle X_{N_2} \rangle \langle X_{Xe} \rangle dx dz}. \quad (23)$$

The angle brackets,  $\langle X_{N_2} X_{Xe} \rangle$ ,  $\langle X_{N_2} \rangle$  and  $\langle X_{Xe} \rangle$ , indicate the averaging of the respective mass fractions in  $y$ -direction. The error  $\Delta \Theta_N$  at a resolution of  $N$  ppr is defined as the difference between  $\Theta_N$  and  $\Theta_{160}$ , normalized by  $\Theta_{160}$ ,

$$\Delta \Theta_N = \frac{|\Theta_N - \Theta_{160}|}{|\Theta_{160}|}. \quad (24)$$

We compare six resolutions,  $N = \{50, 80, 100, 120, 140, 160\}$  ppr, where the highest resolution serves as reference. The shock Mach number, the thermodynamic initial conditions and the bubble diameter are set identical to the main simulations of the presented work. Figure 2 shows the error of the MMF for each resolution. The mixing is one of the main quantities of interest, hence the error due to spatial resolution should be reduced to a minimum. The largest discrepancy can be found during the shock wave passage in the early stage of the interaction ( $t < 100 \mu\text{s}$ ). The lowest resolution of 50 ppr shows an error margin of up to 100%. The increase

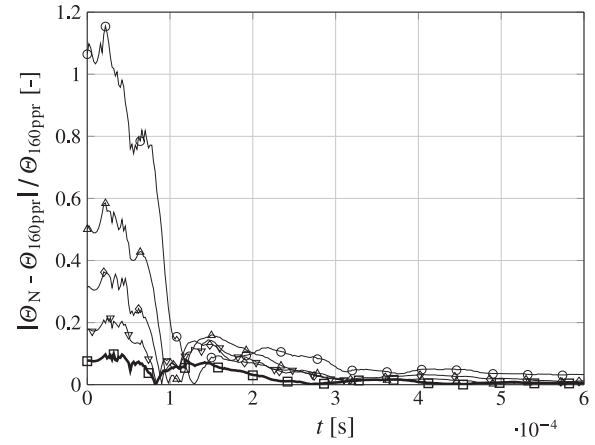


Fig. 2. Convergence of MMF.  $\circ$  : 50 ppr,  $\triangle$  : 80 ppr,  $\diamond$  : 100 ppr,  $\nabla$  : 120 ppr,  $\square$  : 140 ppr.

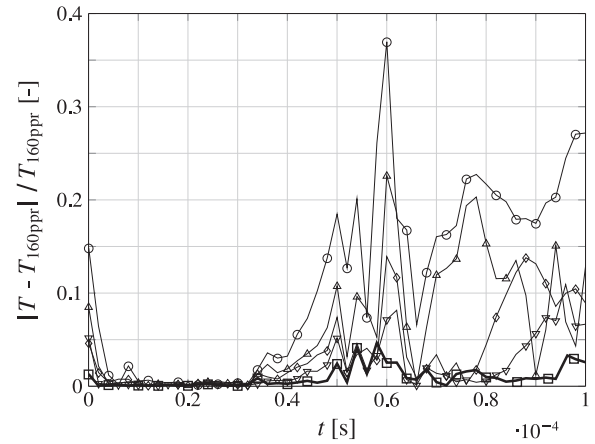


Fig. 3. Convergences of maximum temperature during shock wave passage.  $\circ$  : 50 ppr,  $\triangle$  : 80 ppr,  $\diamond$  : 100 ppr,  $\nabla$  : 120 ppr,  $\square$  : 140 ppr.

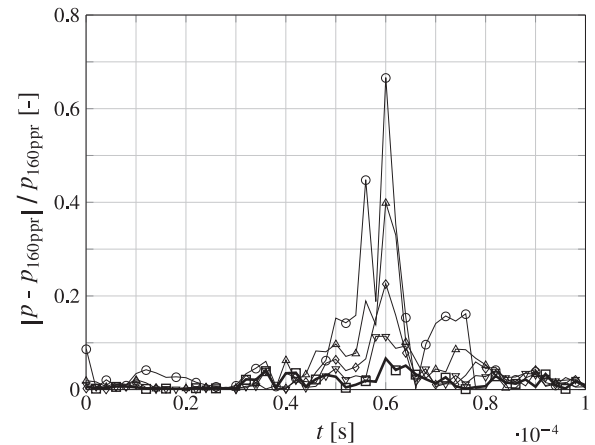
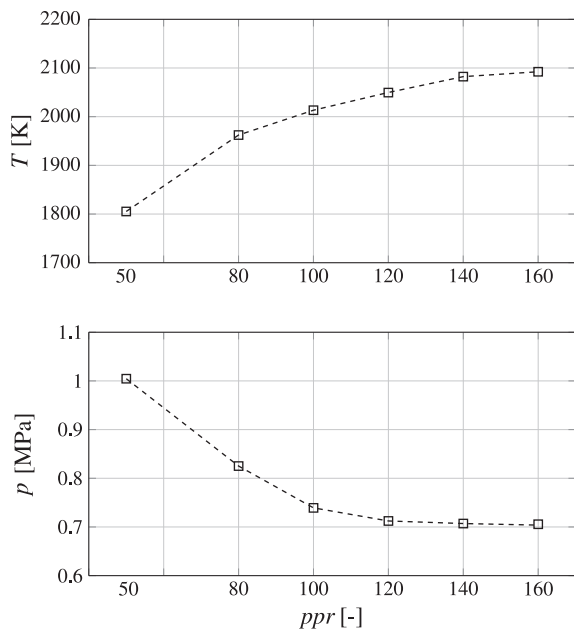


Fig. 4. Convergence of maximum pressure during shock wave passage.  $\circ$  : 50 ppr,  $\triangle$  : 80 ppr,  $\diamond$  : 100 ppr,  $\nabla$  : 120 ppr,  $\square$  : 140 ppr.

of ppr leads to a successive reduction of the error. At a resolution of 140 ppr the error is reduced to less than 10% in the early stage and less than 1% in the long-term evolution of MMF, where the main emphasis of our study lays.

Besides the accurate prediction of MMF, the correct calculation of the pressure and temperature peak during the shock wave passage is important. Especially for RSBI, these two data determine the ignition delay time and the ignition spot. Figures 3 and 4 show the error of the maximum temperature and pressure during the



**Fig. 5.** Temperature and pressure peak for different resolutions at the downstream pole of the bubble during shock focusing.

shock wave passage ( $t < 100 \mu\text{s}$ ). During the shock focusing at  $t \approx 60 \mu\text{s}$  a precise prediction of temperature and pressure is crucial. Similar to the earlier observation for the MMF, the coarse resolution fails in the correct prediction and an increase of ppr reduces the error significantly. At a resolution of 140 ppr, the remaining deviation amounts to only 6% of the maximum pressure and 2.5% of the temperature peak. Figure 5 shows the temperature and pressure peak for the different resolutions at the downstream pole

of the bubble during shock-focusing. Both data exhibit convergent behavior.

Furthermore, the ignition delay time and the location of ignition show convergence at this resolution. The position inside of the bubble where the gas mixture ignites is not affected by a further increase in resolution. In accordance to previous studies, we choose a resolution of 140 ppr for our main simulations of RSBI, which is a higher ppr than used in all previous studies. The important parameters in the field of RSBI, the temperature and pressure peak as well as the molar mixing fraction, show convergence at a resolution of 140 ppr.

## 4. Results and discussion

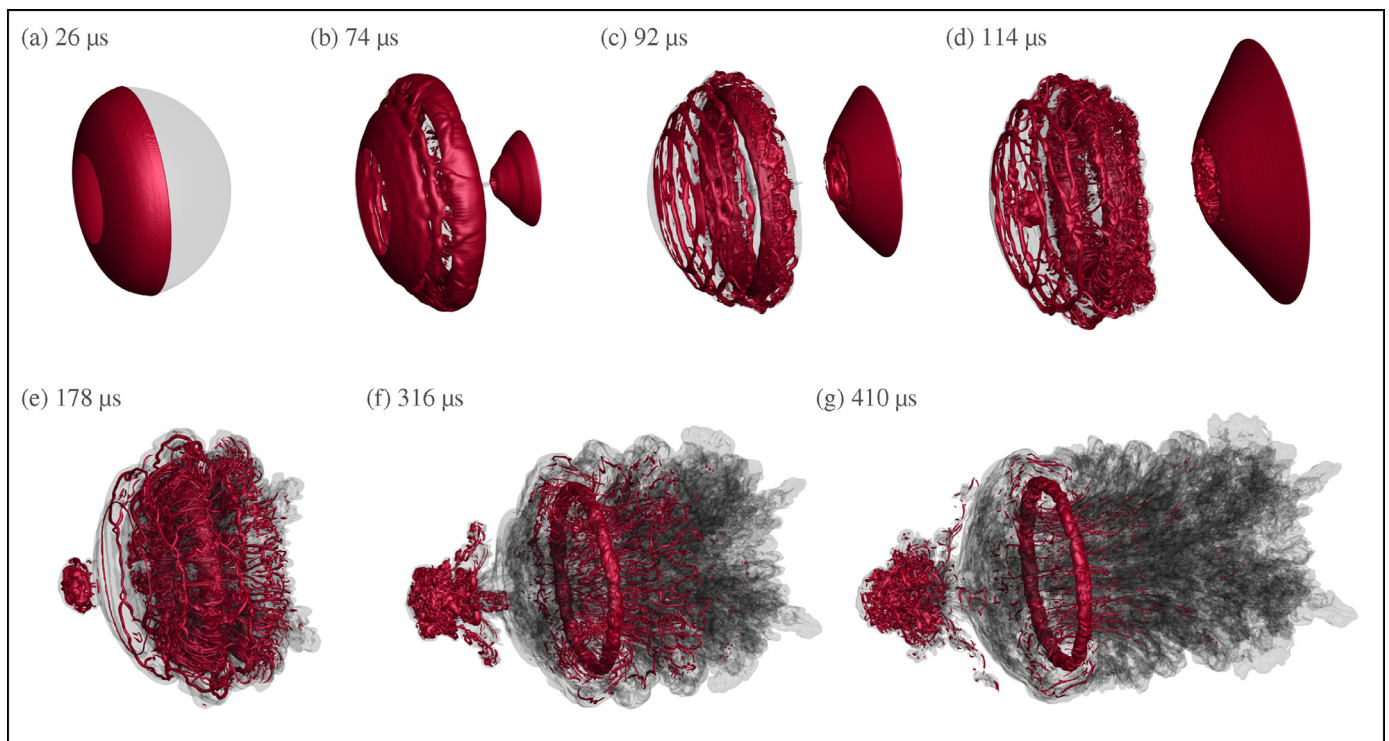
In the following section, we present the results of the RSBI at a shock Mach number of  $Ma = 2.83$ . First we discuss the three-dimensional ISBI and RSBI in detail. We emphasize the effect of the reaction wave by analyzing the spatial and temporal evolution as well as integral quantities. Thereafter the results are compared with results of two-dimensional simulations to quantify the influence of three-dimensional effects on SBI. Finally we compare our results to the experimental data of Haehn et al. [22].

### 4.1. Three-dimensional RSBI

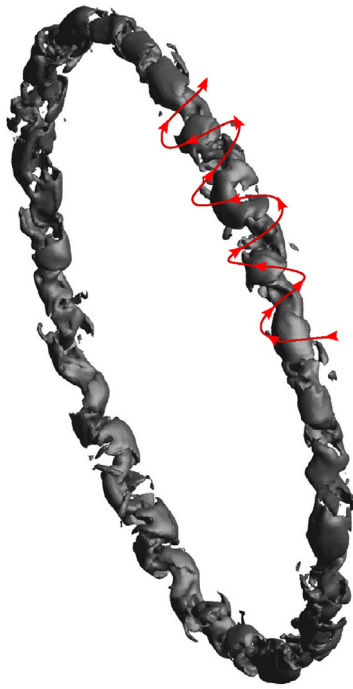
#### 4.1.1. Inert bubble dynamics

Figure 6 shows surface plots at characteristic time instances of an ISBI evolution to illustrate the hydrodynamic effects induced by the interaction between the shock wave and the gas bubble. Iso-surfaces of the mass fraction of xenon are shown in gray and iso-surfaces of the vorticity magnitude are shown in red.

The first plot at  $t = 26 \mu\text{s}$ , Fig. 6(a), shows the bubble during the shock wave passage. Vorticity is produced at the outer interface by the misalignment of the pressure and density gradients



**Fig. 6.** Bubble evolution for ISBI at  $Ma = 2.83$ . The gray translucent isosurface indicates a specific mass fraction of xenon ( $Y_{Xe} = 0.1$ ). The red colored isosurface represents a characteristic value of the vorticity magnitude ( $|\omega| = 400000 \text{ s}^{-1}$ ) to visualize the evolution of the main vortex ring. (For interpretation of the references to color in this figure legend, the reader is referred to the web version of this article.)



**Fig. 7.** Vortex ring with Widnall-type instability in the long-term evolution of ISBI ( $Ma = 2.83$ ) at  $t = 600 \mu\text{s}$ .

(baroclinic vorticity). Figure 6(b) depicts the growth of instabilities at the interface of the bubble at  $t = 74 \mu\text{s}$ . The vorticity isosurface rings indicate regions where the roll-up of the bubble gas is initiated. Already at this early stage of ISBI, the inner vortex ring is visible. This main vortex ring is preserved throughout the entire simulation time range and shows only a slow decay. At late stages of ISBI, shown in Fig. 6(f) and (g), the vortex ring is still visible, whereas the finer vorticity structures at the outer interface have already vanished.

The surface plots at the intermediate stage of ISBI between  $t = 92 \mu\text{s}$ , Fig. 6(c), and  $t = 178 \mu\text{s}$ , Fig. 6(e), are characterized by finer filaments of vorticity, indicating the breakup of the large-scale structures at the bubble interface into smaller vortices. RMI and KHI are fully evolved, which leads to an increase in mixing, amplified by the further roll-up of the shocked bubble gas. Fine filaments of vorticity indicate regions of high vortex stretching and nonlinear energy transfer. Figure 6(e) outlines the filaments inside the roll-ups of the bubble. We also observe the formation and stretching of elongated hairpin-like structures in the azimuthal direction of the vortex core, an effect that can only be resolved in three-dimensional computations. Same observations have been made by Hejazialhosseini et al. [42] in their study of three-dimensional ISBI. Furthermore, as the bubble moves upstream, small ring-like structures are transported into the downstream direction and a jet of the surrounding  $\text{N}_2$  transports high density fluid from the downstream pole into the core of the bubble, which ejects a mushroom-like structure of bubble gas. The blow-out structures are in very good agreement with the experimental results of Ranjan et al. [45], who accelerated a bubble, filled with Ar and surrounded by pure  $\text{N}_2$ , with a shock wave with  $Ma = 2.88$  and observed the same mushroom-like structure at the upstream pole of the bubble.

We observe that the main vortex ring becomes unstable at late stages. Figure 7 shows the vortex ring at  $t = 600 \mu\text{s}$ , destabilized by azimuthal bending modes. Our observations are in very good agreement with the results of Klein et al. [46]. They also observed that their shocked sphere undergoes an azimuthal bending mode

instability, which is analogous to the Widnall instability [47]. An unstable vortex ring due to the growth of azimuthal modes is also reported by Niederhaus et al. [40] in their investigation of vorticity evolution in two- and three-dimensional simulations of ISBI, as well as in the study of Hejazialhosseini et al. [42], analyzing the vortex dynamics in three-dimensional ISBI. Furthermore they observed a restriction for the growth of Widnall-type instabilities: the Atwood number has to be larger than 0.2 to induce the azimuthal instability, which is fulfilled in our setup with an Atwood number of  $A = 0.476$ . The destabilized vortex ring significantly affects the mixing process at late stages of evolution.

#### 4.1.2. Chemically reacting bubble dynamics

The consideration of chemical reaction kinetics in RSBI changes the spatial and temporal bubble evolution significantly. The stoichiometric  $\text{H}_2\text{--O}_2$  gas mixture is compressed and heats up during the shock-wave passage. The convex shape of the bubble increases this effect by shock focusing. The mixture ignites, if at a certain point a sufficient amount of radicals has been formed. Depending on the shock strength, the ignition point moves from the shock-focusing point at the downstream pole of the bubble for low shock Mach numbers up to the upstream pole for high shock Mach numbers [3].

The ignition spot and the propagation of the reaction wave is shown in Fig. 8. Each set of isosurface and isocontour plots contains a two-dimensional slice and a three-dimensional rendering of the RSBI. Figure 8(a) shows the bubble shortly after ignition. The solid line represents the initial shock wave, propagating from left to right. The gas mixture is ignited directly behind the shock wave after a short induction time and propagates as a combustion ring through the bubble gas. At the early stage of combustion the reaction wave spreads radially in all spatial directions, see Fig. 8(b). After approximately  $10 \mu\text{s}$ , the reaction wave has consumed most of the bubble gas and a torus-like region of burned gas is formed, which is outlined in Fig. 8(c). The last set of isosurface and isocontour plots in Fig. 8(d) shows the RSBI at  $t = 100 \mu\text{s}$ . The  $\text{H}_2\text{--O}_2$  mixture has been burned, shock reflections cause a complex temperature field inside the bubble and the roll-up with the formation of the main vortex ring is initiated. The propagation of the detonation wave towards the shock-focusing point and the subsequent blow out of bubble gas leads to a characteristic jellyfish-like structure of three-dimensional RSBI.

For the investigation of the induction and ignition process, we analyze the accumulation of radicals during the shock wave passage, shown in Fig. 9. Exemplary for the five intermediate species, we plot the maximum concentration of the radicals  $\text{HO}_2$  and  $\text{H}_2\text{O}_2$  and the temperature in the early stage of RSBI ( $t < 100 \mu\text{s}$ ). The maximum temperature in the flow field serves as an indicator for the ignition. First radicals are formed directly after the shock wave impacts the bubble ( $t = 2 \mu\text{s}$ ). Thereafter the mass fractions of  $\text{HO}_2$  and  $\text{H}_2\text{O}_2$  increase slightly until  $t = 38 \mu\text{s}$ , however the production rates are insufficient to ignite the gas mixture or to start a chain reaction. At  $t = 38 \mu\text{s}$ , the initial shock wave reaches the ignition point and the induction phase starts. We observe a sudden increase in the formation of the radicals accompanied by a slight temperature rise. The chain reaction starts and finally ignites the gas mixture at  $t = 42 \mu\text{s}$ . The following reaction wave propagates through the bubble gas and has burned the stoichiometric mixture at  $t = 56 \mu\text{s}$ . The slight decline of the maximum temperature indicates the termination of the main reaction. Further fluctuations of the radicals and the temperature are caused by shock waves, which re-induce some weak reactions to sustain the chemical equilibrium.

Figure 10 compares the spatial and temporal bubble evolution between three-dimensional RSBI (left column) and ISBI (right column). The slices depict the density in the upper parts and the mix-

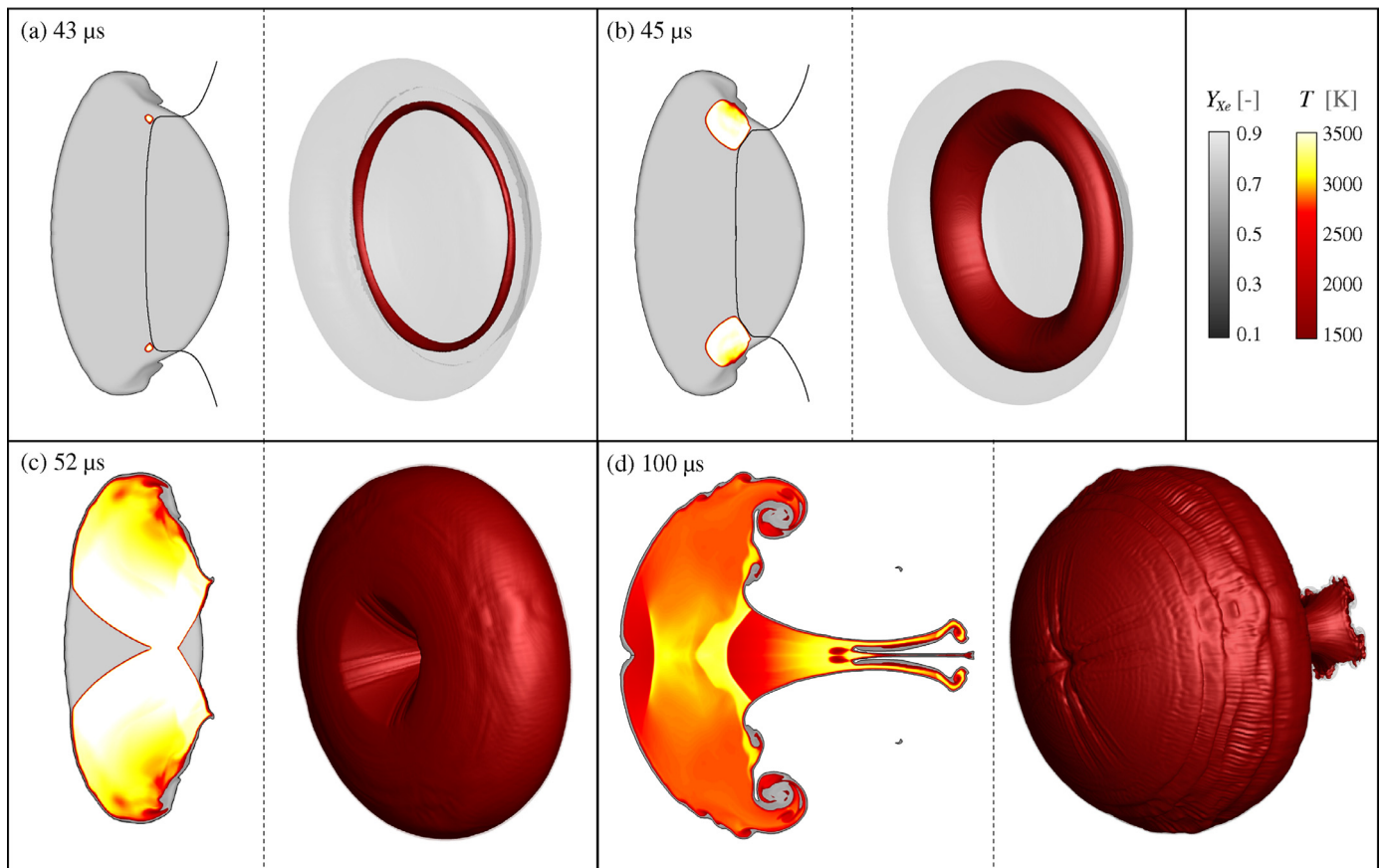


**Fig. 8.** Ignition and detonation wave propagation in a RSBI with a shock Mach number of  $Ma = 2.83$ . For two-dimensional plots: Gray color scale shows the xenon mass fraction, red–yellow color scale the temperature with a cutoff at  $T = 1500$  K. Black lines in (a) and (b) depict the initial shock wave, propagating from left to right. For three-dimensional plots: red isosurface depicts the temperature at cutoff level of  $T = 1500$  K, gray isosurface illustrates the bubble shape ( $Y_{Xe} = 0.1$ ). (For interpretation of the references to color in this figure legend, the reader is referred to the web version of this article.)

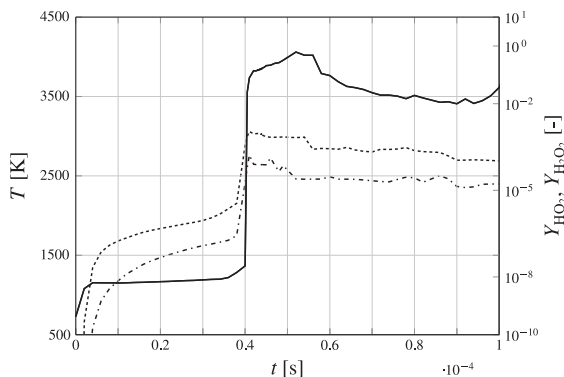


**Fig. 9.** Maximum temperature and radical mass fractions during the early stage of RSBI, including induction time, ignition and reaction wave propagation. —: temperature; .....:  $Y_{HO_2}$ ; .....:  $Y_{H_2O_2}$ .

ing between the inert gas Xe and the surrounding gas  $N_2$  in the lower part ( $Y_{N_2} \cdot Y_{Xe}$ ). The bubble gas is highly mixed with the surrounding gas in dark colored zones and less mixed in regions with lighter color. In addition the mass fraction peak of hydroperoxyl radicals illustrate the reaction wave front. During the compression and ignition stage of the RSBI, outlined in Fig. 10(a), no influence of the chemical reaction kinetics on the bubble evolution is visible. The spatial expansion is initially influenced after the reaction wave reaches the interface, see Fig. 10(b). Thereafter, the growth of secondary instabilities is significantly affected. Figure 10(c) shows

the early growth stage of KHI at the outer interface for the ISBI, whereas the RSBI lags of these instabilities. The detonation wave damps the growth of KHI as well as the formation of the vortex core. There are two reasons for this deceleration: The detonation wave induces vorticity with opposite sign compared to the vorticity produced by the initial shock wave and thus reduces the total vorticity at the interface. Additionally, increased molecular diffusion across the reaction wave reduces the growth rate of the instabilities. The temperature increase across the reaction front and the spatial expansion decreases the density and increases the viscosity of the bubble gas. The fourth contour plot, Fig. 10(d), shows that the density of the bubble gas is even lower than the surrounding gas, which is in contrast to the inert SBI, where the density of the bubble gas is significantly higher than the density of the surrounding  $N_2$ . Figure 10(c) and (d) illustrate the blow-out of bubble gas and the formation of the jellyfish-like structure of RSBI, characterized by a smoother, less mixed, interface compared to the inert SBI. The last set of contour plots (e) at  $t = 450 \mu s$  shows the long-term spatial evolution of the inert and reacting bubble. The two simulations clearly differ: RSBI on the left side is characterized by the blow-out of large amounts of bubble gas in downstream direction, forming a nozzle-like structure. Surrounding gas is transported along the center axis in upstream direction and penetrates the gas bubble. Strong mixing takes place near the vortex ring and in the upstream region. However, most of the bubble gas in the downstream region is nearly unmixed. The ISBI shows a different evolution, large areas of the bubble are mixed with the surrounding. The unimpeded growth of instabilities accelerates the mixing especially in the downstream part and in the blow-out region at

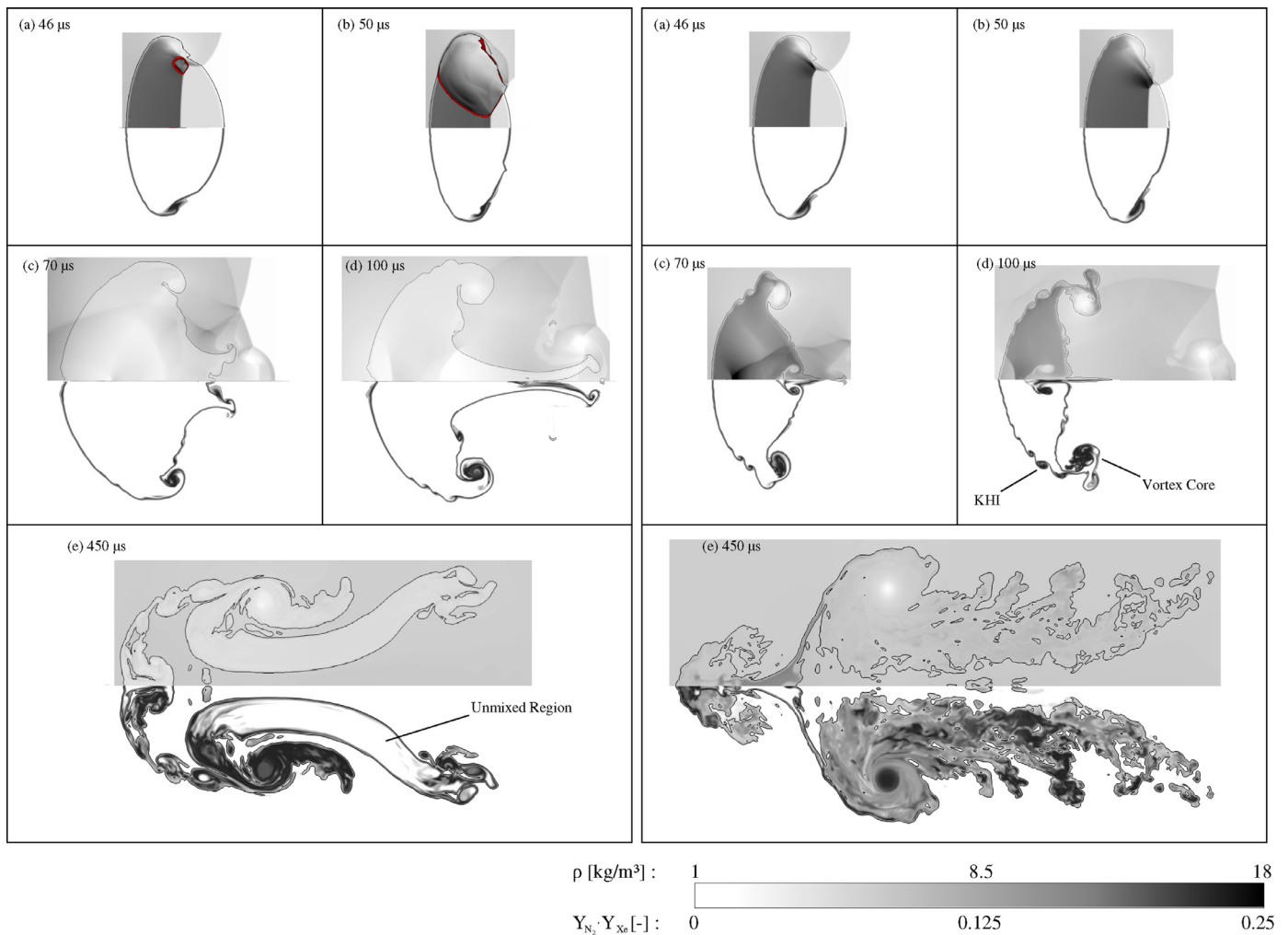


**Fig. 10.** Evolution of three-dimensional RSBI (left) and ISBI (right). Isolines of  $Y_{Xe} = 0.1$  outlines the bubble interface. The contour plot shows density (top) and mixing of the two inert gases (bottom) for five instants. The reaction wave front is indicated by the peak of  $Y_{H_2O}$ , in red color scale (first two contour plots on the left side). (For interpretation of the references to color in this figure legend, the reader is referred to the web version of this article.)

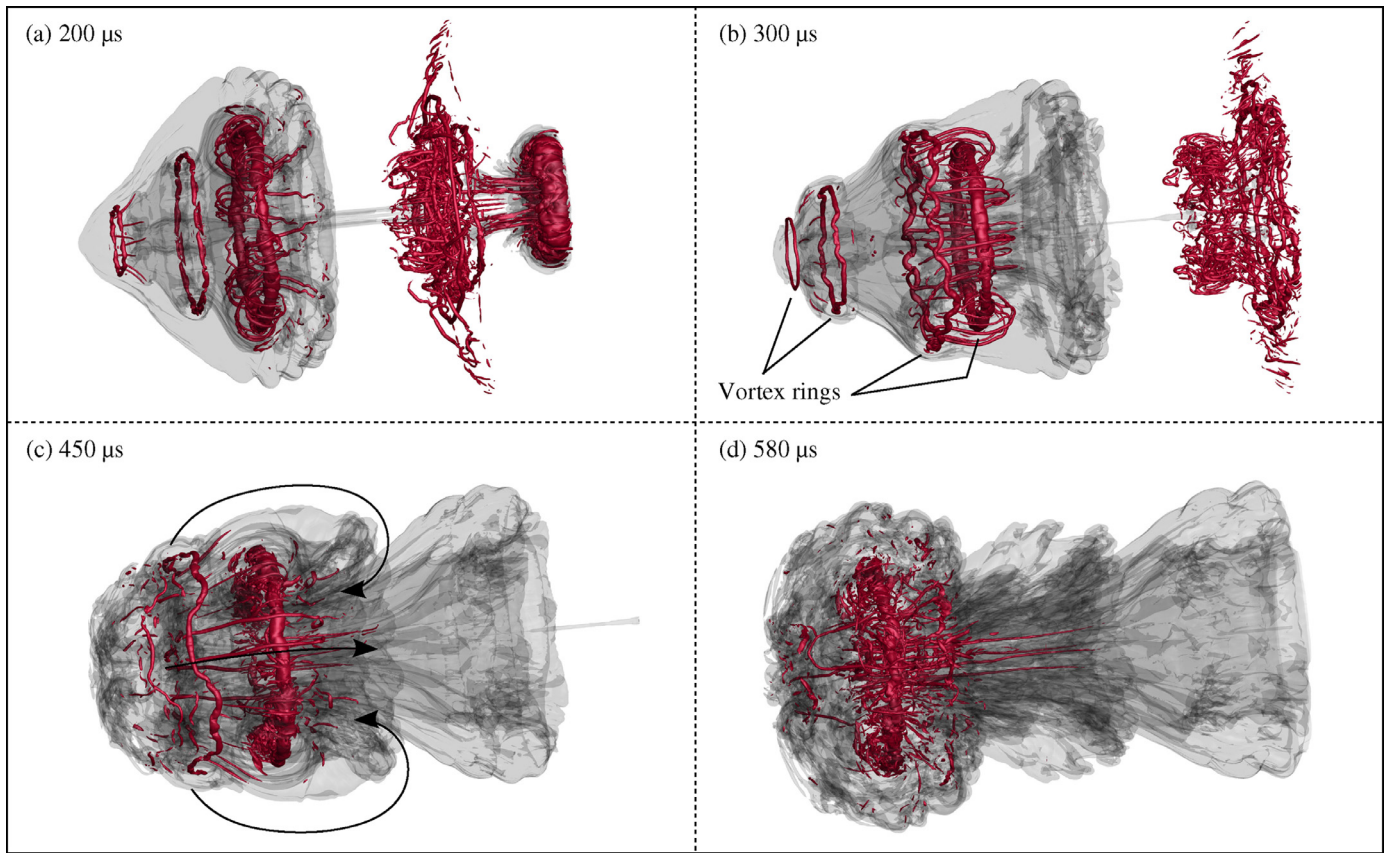
the upstream pole of the bubble, only the throat region exhibits small amounts of unmixed bubble gas.

Figure 11 shows the temporal evolution of regions with high vorticity in the RSBI at four characteristic time steps. In contrast to the ISBI shown in Fig. 6, which is characterized by a highly mixed bubble gas with a large number of fine filaments of vorticity, the surface plots of the RSBI show that vorticity is concentrated inside the bubble in form of several distinct vortex rings. Despite the chemical reaction and the different spatial bubble evolution, we observe a similar main vortex ring as in ISBI, however, with a slightly smaller diameter. Beside the main vortex ring, the RSBI shows three additional vortex rings (Fig. 11(b)), whereas the one with the largest diameter shows a highly unstable behavior already at  $t = 300 \mu\text{s}$ . The three additional vortex rings are transported downstream and circulate around the main vortex ring. They are characterized by a successive decay, the largest vortex ring has vanished completely at  $t = 450 \mu\text{s}$ , see Fig. 11(c). Figure 11(d) shows the vortex rings at  $t = 580 \mu\text{s}$ ; the tail of the shocked bubble is transported further downstream and the additional vortex rings are dispersed into small filaments of vorticity. Only the main vortex ring persists, however, with a strongly disturbed structure. Furthermore, we observe a roll-up of the bubble gas around the vortex ring (illustrated with a set of arrows in Fig. 11(c)) and the growth of instabilities in the upstream region around the vortex ring. The animation available with the online version of the paper

shows the rotation of the smaller vortex rings around the main vortex ring and clarifies the temporal decay.

#### 4.1.3. Transverse bubble diameter

The reaction wave has a distinct influence on the spatial expansion of the bubble. To quantify the impact of the chemical reaction, we analyze the normalized transverse bubble diameter (TBD), which is defined as  $\tilde{\Lambda}_y = \Lambda_y/D_0$ . The TBD describes the maximum spatial expansion of the bubble gas in transverse direction ( $\Lambda_y$ ), normalized by the initial bubble diameter  $D_0$ . The bubble diameter  $\Lambda_y$  is measured based on a threshold value of the xenon mass fraction of  $Y_{Xe} = 0.01$ . Figure 12 depicts the temporal evolution of TBD for ISBI (solid line) and RSBI (dashed line). Contour plots of the bubble at three characteristic time steps are plotted in Fig. 13, showing the mass fraction of Xe to illustrate the different shape of ISBI and RSBI. The bubble diameters of the two simulations are identical at the early stage of the evolution. The shock wave compresses the bubble gas and hence the TBD is reduced. At  $t = 42 \mu\text{s}$  the reactive gas mixture is ignited and the subsequent reaction wave leads to a significant expansion of the bubble gas. The first contour plots (a) in Fig. 13 show the expansion at  $t = 100 \mu\text{s}$ . The point in time where the RSBI shows the highest  $\tilde{\Lambda}_y$ . The temperature rise and density decrease across the reaction front leads to a higher bubble volume, compared to the ISBI. Thereafter, the TBD of the RSBI decreases and large compact parts of the bubble gas are



**Fig. 11.** Vortex ring evolution for RSBI at four characteristic timesteps. Gray translucent isosurface shows a specific mass fraction of xenon ( $Y_{Xe} = 0.1$ ). The red isosurface represents a characteristic value of the vorticity magnitude ( $|\omega| = 400,000 \text{ s}^{-1}$ ) to visualize the evolution of the vortex structure, including the main vortex ring. (For interpretation of the references to color in this figure legend, the reader is referred to the web version of this article.)

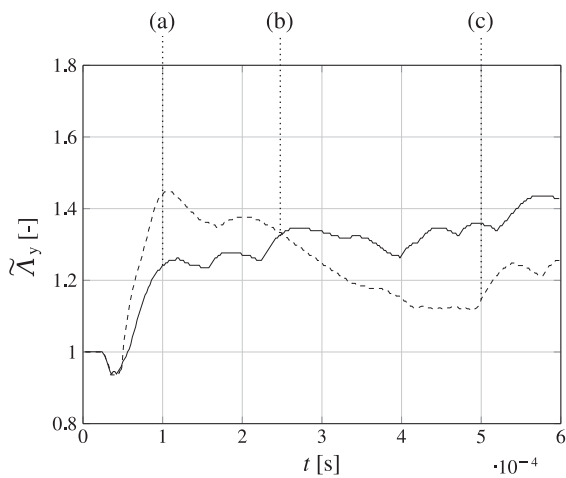


**Fig. 12.** Normalized transverse bubble diameter for three-dimensional ISBI and RSBI. —: non reacting; - - -: reacting.

transported downstream. In contrast, the TBD of the ISBI shows a different behavior: Figure 12 shows a continuous increase of the bubble diameter over time, the high vorticity leads to a successive expansion in transverse and downstream direction. The inert and reacting TBDs intersect at  $t = 244 \mu\text{s}$ . The contour plots, Fig. 13 (b), reveal that the vortex ring of the ISBI is more outbound and developed than the reacting counterpart. In the long-term evolution, Fig. 13(c) at  $t = 500 \mu\text{s}$ , the ISBI shows a highly mixed bubble gas, which has spread in the streamwise as well as in the transverse

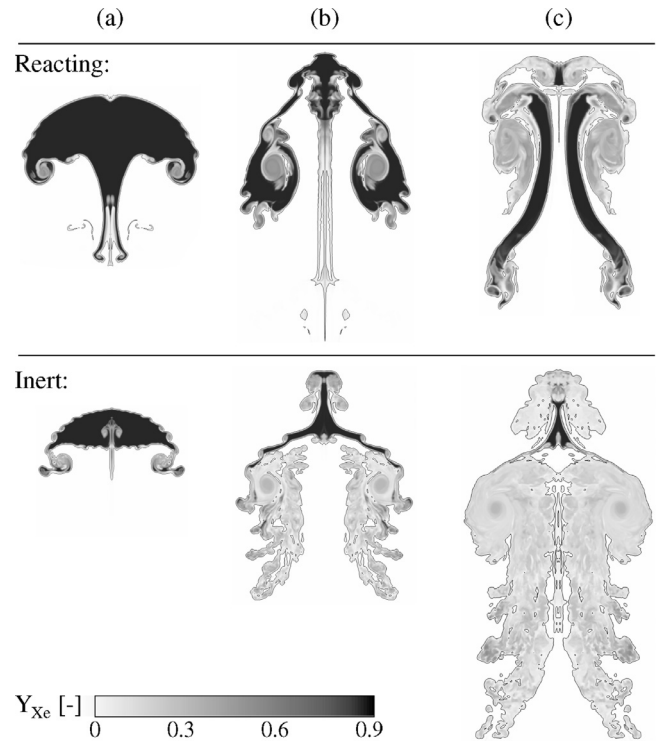


**Fig. 13.** Characteristic contour plots for three-dimensional ISBI and RSBI. Gray color scale indicates the mass fraction of Xe ( $Y_{Xe}$ ). (a):  $t = 100 \mu\text{s}$ ; (b):  $t = 244 \mu\text{s}$ ; (c):  $t = 500 \mu\text{s}$ .

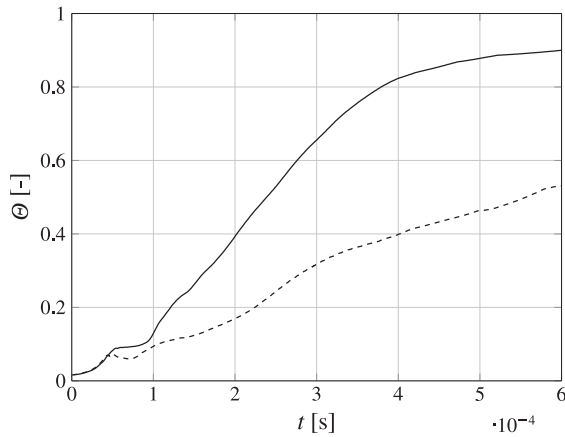


Fig. 14. Molar mixing fraction for three-dimensional ISBI and RSBI. —: inert; .....: reacting.

direction. The RSBI shows a more complex behavior: the TBD is reduced until  $t = 400 \mu\text{s}$ , the diameter of the main vortex ring decreases and determines the maximum spatial expansion. Thereafter, the diameter of the vortex ring is smaller than the diameter of the nozzle-like structure in the downstream part of the bubble for approximately  $100 \mu\text{s}$ . This structure remains stable and therefore the TBD stays nearly constant. However, after  $t = 500 \mu\text{s}$  the roll-up of the bubble gas around the vortex ring leads to a spatial expansion and an increase of the TBD. We outline both stages; Fig 11(c) shows the RSBI before the roll-up with a maximum TBD in the nozzle-like region and Fig 11(d) during the roll-up of the bubble gas and the subsequent increase in the diameter at the upstream regions of the shocked bubble.

#### 4.1.4. Mixing in RSBI

The results shown in Figs. 10–13 have indicated distinct deviations in the mixing behavior of the bubble gas between ISBI and RSBI. For quantification, we analyze the temporal evolution of the molar mixing fraction (MMF) in Fig. 14, as defined in Eq. (23) in Section 3.2. During the early stage of the simulations, the MMF shows the same increase for both cases. The molar mixing fraction differs only after the ignition of the bubble gas. The MMF of the ISBI increases during the shock wave passage and levels for approximately  $\Delta t = 40 \mu\text{s}$ . Within this period, the shock-induced secondary instabilities start to evolve. After their formation, they contribute significantly to the MMF, which increases linearly for the next  $250 \mu\text{s}$ , followed by a leveling at approximately  $\Theta = 0.9$ . This integral quantity confirms the observation of a highly mixed bubble gas, based on the three-dimensional isosurface plots of the ISBI in Fig. 6. The RSBI shows a different evolution: after ignition, the subsequent detonation wave flattens the bubble interface and decreases the MMF slightly. Thereafter, mixing increases, but with a significant lower rate compared to the inert counterpart. Similarly to ISBI, secondary instabilities act as a main driver of mixing, however, due to the detonation wave, these instabilities exhibit a different evolution. As shown in the contour plots in Fig. 10, the growth of instabilities is decelerated by the reaction wave, leading to a lower MMF the RSBI. At the end of the simulated time range, the RSBI MMF amounts to approximately  $\Theta = 0.53$ . Large regions of unmixed bubble gas remain, especially in the nozzle-like structure in the downstream region. In total, mixing is reduced by up to 40% compared to the inert case.

#### 4.2. Comparison with two-dimensional simulations

In the following section, we compare the three-dimensional results to two-dimensional simulations at the same shock Mach

number of  $Ma = 2.83$ . We use the same grid resolution for both simulations. Differences are expected, particularly at late stages of SBI evolution. Figure 15 shows contour plots at characteristic stages; the left box contains the two-dimensional plots and the right box the three-dimensional results. The isocontour lines of  $Y_{Xe} = 0.1$  illustrate the bubble interface and indicate the interface deformation pattern. The upper parts of Fig. 15 outline the density, the lower part the vorticity magnitude. The first plots (a) show no differences between two- and three-dimensional simulations during the shock wave passage at  $t = 66 \mu\text{s}$ . During the growth stage of the KHI, annotated in the second contour plots (b), no three-dimensional effects can be observed at the outer interface. First differences become visible during the intermediate ISBI stage, see Fig. 15(c) and (d). The vorticity in the two-dimensional simulation coalesces in a compact vortex ring. A vortex pair propagates in the upstream direction, followed by a jet of  $N_2$  in the center axis of the bubble. The  $N_2$ -jet is shown in the magnified sections in Fig. 15(c), detail and Fig. 15(d), detail (left column). The three-dimensional simulation shows a different evolution: The vortex ring is in a more outbound position and less compact. We observe a higher degree in mixing already in the intermediate stage of ISBI and the growth rates of the KHI are decelerated. Furthermore, the  $N_2$ -jet is absent; however, a jet of bubble gas is formed and propagates in the upstream direction, resulting in a mushroom-like structure in the long-term evolution, see Fig. 15(e). The missing jet was also reported by Giordano and Burtshell [48] in their study of RMI in two- and three-dimensional ISBIs. The long-term evolution is dominated by the effect of the vortex stretching term, which is absent in two-dimensional simulations. Vortex stretching leads to an elongation of the bubble gas in streamwise direction. The contour plots emphasize the different evolution of two- and three-dimensional simulations in the late stage of ISBI. The flow field shows large discrepancies in terms of spatial expansion and mixing. The isocontour lines of xenon show a cloud of mixed bubble gas for the three-dimensional domain, containing complex turbulent structures. The two-dimensional simulation preserves a sharp interface between the shocked bubble and the surrounding, especially at the outer interface. Obviously two-dimensional simulations cannot reproduce Widnall-type instabilities, which are responsible for the destabilization of the vortex ring in the long-term evolution [49]. This results in a less mixed structure of the shocked bubble at the late stages of two-dimensional SBI.

The normalized bubble diameters for ISBI and RSBI calculated from two- and three-dimensional simulations are plotted in Fig. 16 and support the observation from the contour plots in Fig. 15. The diameters for the inert simulations ( $\circ$ ) are nearly identical until  $t = 70 \mu\text{s}$ , thereafter the evolution differs. Both diameters increase in time, however with different slopes: The three-dimensional SBI (solid line) is characterized by a lower slope compared to the two-dimensional setup (dashed line), which leads to a successive divergence of the bubble diameters. This observation is in accordance with previous studies: Wang et al. [50] also measured a smaller bubble diameter in their study of three-dimensional ISBI in comparison with two-dimensional ISBI. These differences are caused by the missing vortex stretching in two dimensions, which reduces the spanwise expansion in the long-term evolution. Hejazialhosseini et al. [42] examined the vorticity growth rates during ISBI at different shock Mach numbers and also emphasized the importance of the vortex stretching term for the expansion in the long-term evolution. The TBD confirms the qualitative analysis of the spatial and temporal bubble evolution in Fig. 15.

RSBI ( $\square$ ) also show a different evolution in two-dimensional and three-dimensional simulations. The bubble diameter evolves similarly at the early stage and exhibits the same ignition delay time, which confirms that the induction time is not significantly affected by three-dimensional effects. However, the subsequent

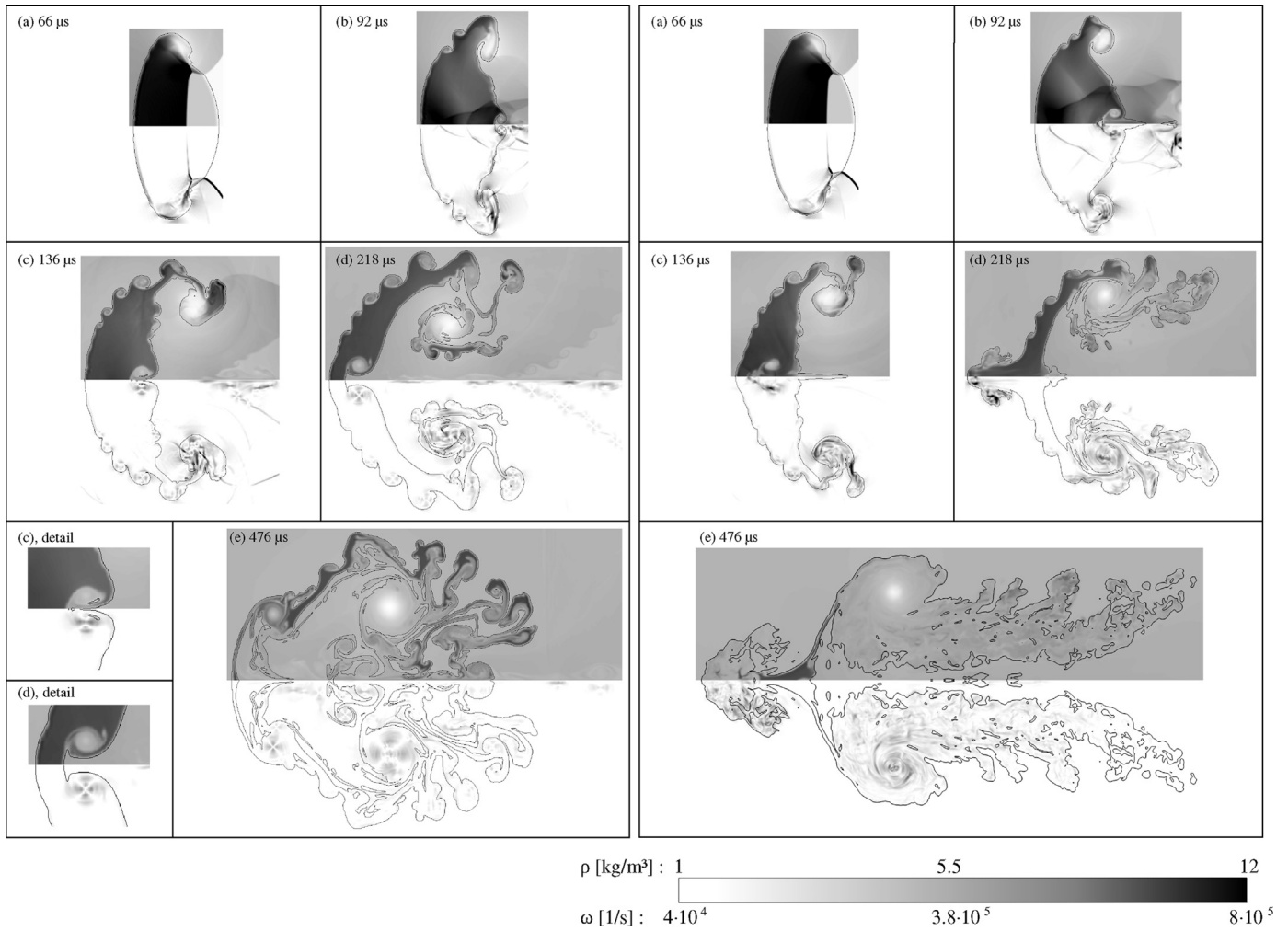


**Fig. 15.** Bubble evolution of two-dimensional (left) and three-dimensional (right) simulations of ISBI at a shock Mach number of  $Ma = 2.83$ . Isocontours of  $Y_{Xe} = 0.1$  outlines the bubble interface. Density (top) and vorticity magnitude (bottom) show different evolution at five time steps.  $N_2$ -jet is illustrated in the magnified sections in (c), detail and (d), detail.

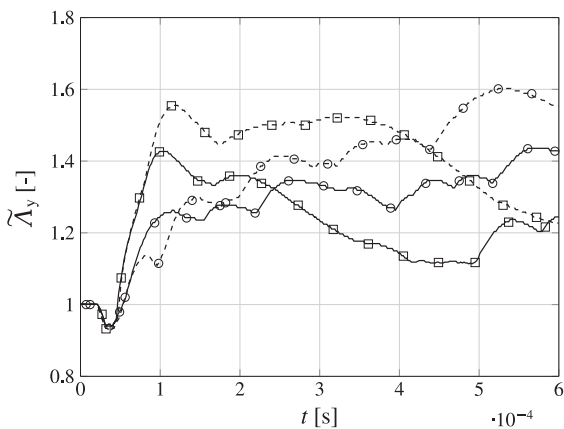


**Fig. 16.** Comparison of TBD for two- and three-dimensional SBI. —: three-dimensional simulations; .....: two-dimensional simulations; ○: ISBI; □: RSBI.

expansion of the reacted bubble gas differs: the two-dimensional simulations leads to a 10% higher expansion. The following temporal evolution is similar, both TBD decrease. However, the two-dimensional RSBI shows a slower reduction, which increases the divergence until  $t = 400 \mu s$ . Thereafter, the TBD is constant and

increases again after  $t = 500 \mu s$ , caused by the roll-up of the bubble gas around the main vortex ring. This effect is absent in two dimensions, see Section 4.1.2. Similarly to the inert simulations, the missing vortex stretching term causes a different spatial evolution. Especially between  $t = 40$  and  $120 \mu s$ , where the TBD diverges, the vortex stretching term exhibits the highest magnitude in the three-dimensional simulation.

The influence of the additional dimension on the mixing is shown in Figure 17 for the MMF of ISBI and RSBI. The mixing is highly influenced by the additional dimension for both cases. The inert simulations show an increase in mixing during the early stages of the shock wave passage,  $t < 50 \mu s$ , and leveling during the shock focusing. Then the mixing raises again, where the three-dimensional ISBI shows a much higher slope than the two-dimensional ISBI, which leads to a higher overall mixing. In the long-term evolution of the three-dimensional ISBI, the bubble is highly mixed and eventually levels out at a MMF of about 90%. The two-dimensional ISBI shows a mixing of approximately 70% at the end of the simulated timeframe, still exhibiting a positive slope, which indicates that the mixing may further increase in time. The better mixing can be explained by the instability of the vortex ring, which contributes to an enhancement in mixing. This effect was also observed by Klein et al. [46] in their investigation of the interaction of strong shock waves with interstellar clouds. Furthermore, the three-dimensional stretching term increases the spanwise

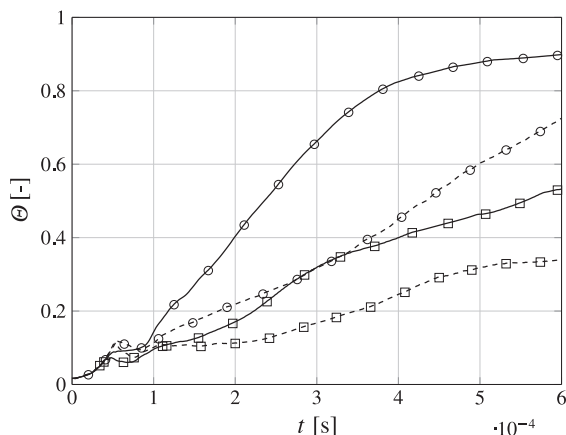


**Fig. 17.** Comparison of MMF for two- and three-dimensional SBI. —: three-dimensional simulations; .....: two-dimensional simulations; ○: ISBI; □: RSBI.

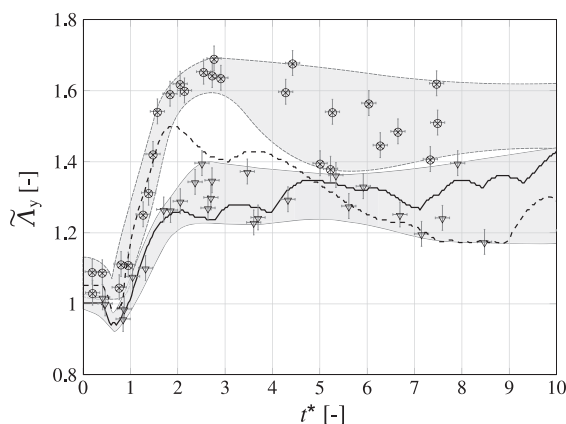


**Fig. 18.** Comparison of TBD for three-dimensional SBI and experimental data. —: ISBI; .....: RSBI; ▽: ISBI; ○: RSBI.

expansion of the bubble gas and contributes to the higher degree in mixing. RSBI shows only weak similarity to the inert counterpart: the three-dimensional simulation shows also a higher mixing than the two-dimensional RSBI. At the end of the simulated timeframe the mixing of the three-dimensional simulation amounts to approximately 53%, which is lower than for the three-dimensional ISBI. The MMF of the two-dimensional RSBI amounts only to about 35% and starts to level at the end of the simulated timeframe.

#### 4.3. Comparison with experimental data

We compare simulation data with experimental results of Haehn et al. [22]. The nominal initial conditions of their experiments are identical to our numerical setup. Figure 18 shows the TBD for the inert and reacting simulation and the experimental data. The experimental data are provided with the normalized time,  $t^* = (tW_i)/D_0$ , which is retained for the plots in Fig. 18 and Fig. 19. The normalization uses the hydrodynamic time scale  $\tau_H$ , which is defined as  $\tau_H = D_0/W_i$ , with the initial bubble diameter  $D_0$  and the incident shock wave speed  $W_i$ . The experimental data contain large uncertainties in time and space and are an ensemble average from several realizations. The scattering between the different experiments is indicated by the gray shaded area. The inert simulation (solid line) agrees well with the experimental data (▽). The decrease of the bubble diameter by the compression of the shock wave at  $t^* \approx 0.8$  is resolved as well as the subsequent expansion of the bubble gas in spanwise direction. After  $t^* > 2$  the main expansion is completed and the TBD increases only slightly

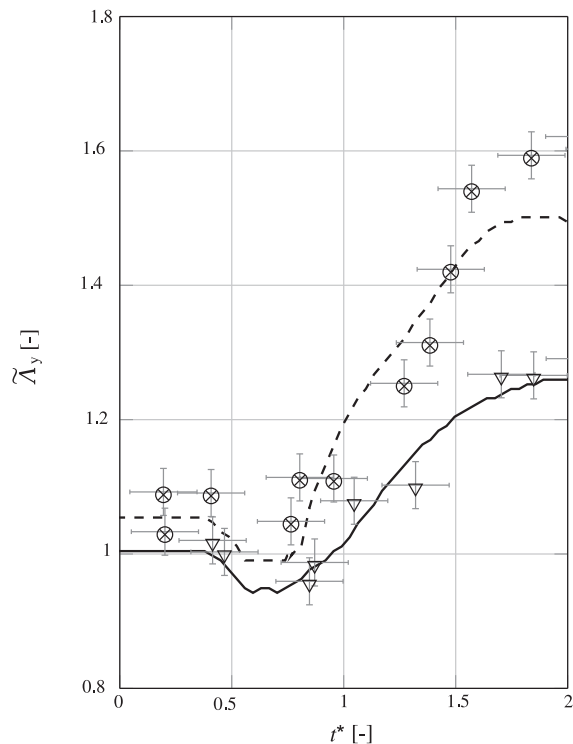


**Fig. 19.** Detailed section of the early stage of TBD for three-dimensional SBI and experimental data. —: ISBI; .....: RSBI; ▽: ISBI; ○: RSBI.

in time, which also is in good agreement with the measured spanwise length of the bubble.

The comparison of the TBD for the RSBI is less conclusive. The experimental pre-shock bubble diameter deviates up to 9% from the nominal diameter. Hence, we adjusted our initial bubble diameter to the average of the measured values of Haehn et al. [22]. The sudden expansion in the early stage until  $t^* = 2$ , induced by the detonation wave, shows very good agreement. Figure 19 outlines the ignition and expansion stage in detail. The slope of the diameter increase agrees very well, which indicates that the propagation velocity of the reaction waves are identical. Thereafter, the increase of the experimentally measured TBD continues, whereas the numerical simulation predicts a slight decrease. Unfortunately, the available data of Haehn et al. [22] do not include the roll-up stage of the RSBI,  $t^* > 9$ . The deviation of the RSBI bubble diameter may be attributed to several reasons. The challenging experimental measurement of the spanwise length of the reacted bubble gas leads to a high scattering. Besides the deviation of the pre-shock bubble diameter of up to 9% from the nominal value, the burned bubble gas shows a large scatter on the long-term evolution, which can be explained by the sensitivity of the chemical reaction kinetics on the gas composition and on the shock Mach number. Haehn et al. [22] quantified the uncertainty of the initial shock Mach number to  $\pm 0.03$  and the uncertainty in the gas mixture composition to  $\pm 3\%$ . Both variations influence the ignition delay and, more importantly, the ignition location significantly. Tritschler et al. [37] performed a detailed uncertainty analysis of two-dimensional ISBI and showed that already small deviations in the initial gas composition highly affect the bubble evolution. Furthermore, the deviation from the nominal initial bubble diameter influences the SBI. Zou et al. [51] studied different bubble aspect ratios in a ISBI and revealed a distinct impact on the spatial bubble evolution, the vorticity production and the vortex ring diameter. Similar observation have been made by Georgievskiy et al. [52].

They studied spherical and slightly stretched bubbles and observed a distinct influence on the thermodynamic post shock properties.

The position of the ignition and the resulting direction of the detonation wave influence the spatial expansion of the bubble significantly. We assume that the ignition in our simulation occurs at a slightly different position than in the experiment, which leads to a small deviation in the propagation direction. The detonation wave of the experimental RSBI spreads partially in the transverse direction, whereas the reaction wave in our simulations mainly propagates in the streamwise direction, which leads to a lower TBD in the simulations. We believe that the TBD has a high sensitivity to the ignition spot, respectively to the shock Mach number and the bubble shape. A set of two-dimensional simulations with slightly different shock Mach numbers confirms this assumption. Deviations of the shock strength in the range of  $Ma \pm 0.03$ , which is within the nominal uncertainty of the experimental data, have a strong effect on the TBD. A detailed uncertainty quantification is beyond the scope of the presented work and recommended for prospective investigations. Nevertheless, the reaction wave speed and the spatial bubble expansion of ISBI confirm the very good overall agreement of our simulation with the experimental data.

## 5. Conclusion

We have presented three-dimensional numerical simulations of a reacting shock–bubble interaction (RSBI) with detailed  $H_2$ – $O_2$  chemical reaction kinetics. A shock wave with a Mach number of  $Ma = 2.83$  accelerates a gas bubble, filled with a stoichiometric gas mixture of  $H_2$  and  $O_2$ , diluted by Xe. During the shock wave passage, the initial shock wave is reflected, transmitted and diffracted, which triggers the Richtmyer–Meshkov and secondary instabilities. Furthermore, the passage of the shock leads to a compression of the bubble gas and a sudden jump in the thermodynamic properties, sufficient to ignite the reactive gas mixture. The following reaction wave in turn interacts with the bubble interface and affects the spatial and temporal evolution as well as the mixing of the bubble gas.

Ignition of the bubble gas is observed upstream of the downstream pole of the bubble. The shock wave is sufficiently strong to ignite the mixture without additional compression in the shock-focusing point. The following reaction wave is a supersonic detonation wave, which suppresses the growth of secondary instabilities and reduces mixing by up to 40% compared to the inert simulation. Furthermore, the reaction wave decreases the spatial expansion in the transverse as well as in the streamwise direction.

The comparison of three- and two-dimensional RSBI reveals the distinct influence of three dimensional effects on the bubble evolution. We observed differences in the long-term evolution: the two-dimensional vortex core remains stable, whereas the three-dimensional vortex ring is destabilized by Widnall-type instabilities. The vortex stretching term, which is absent in two-dimensional simulations, increases the spatial bubble expansion of the three-dimensional simulation in the streamwise direction. Both effects, the breakdown of the vortex ring and the vortex stretching, increase the mixing significantly. Furthermore, comparison with experimental data showed very good agreement in terms of ignition delay time, reaction wave propagation velocity and spatial expansion rate. While a detailed quantification of parametric uncertainties was not the goal of this paper, we recommend further exploration of the effect of initial-data uncertainties on the long-term evolution for future work.

## Acknowledgment

The authors gratefully acknowledge the Gauss Centre for Supercomputing e.V. (<http://www.gauss-centre.eu>) for funding this

project by providing computing time on the GCS Supercomputer SuperMUC at Leibniz Supercomputing Centre (LRZ, <http://www.lrz.de>).

This project has received funding from the European Research Council (ERC) under the European Union's Horizon 2020 research and innovation programme (grant agreement No 667483).

## Supplementary material

Supplementary material associated with this article can be found, in the online version, at [10.1016/j.combustflame.2017.03.026](https://doi.org/10.1016/j.combustflame.2017.03.026).

## References

- [1] D. Ranjan, J. Oakley, R. Bonazza, Shock–bubble interactions, *Annu. Rev. Fluid Mech.* 43 (1) (2011) 117–140.
- [2] F.R. Diegelmann, V. Tritschler, S. Hickel, N.A. Adams, On the pressure dependence of ignition and mixing in two-dimensional reactive shock–bubble interaction, *Combust. Flame* 163 (2016) 414–426.
- [3] F.R. Diegelmann, S. Hickel, N.A. Adams, Shock Mach number influence on reaction wave types and mixing in reactive shock–bubble interaction, *Combust. Flame* 174 (2016) 085–099.
- [4] W.D. Arnett, The role of mixing in astrophysics, *Astrophys. J. Suppl.* 127 (2000) 213–217.
- [5] A.M. Khokhlov, E.S. Oran, G.O. Thomas, Numerical simulation of deflagration-to-detonation transition: the role of shock–flame interactions in turbulent flames, *Combust. Flame* 117 (1–2) (1999) 323–339.
- [6] R.S. Craxton, K.S. Anderson, T.R. Boehly, V.N. Goncharov, D.R. Harding, J.P. Knauer, R.L. McCrory, P.W. McKenty, D.D. Meyerhofer, J.F. Myatt, A.J. Schmitt, J.D. Sethian, R.W. Short, S. Skupsky, W. Theobald, W.L. Krueer, Direct-drive inertial confinement fusion: a review, *Phys. Plasmas* 22 (11) (2015) 110501.
- [7] R.D. Richtmyer, Taylor instability in shock acceleration of compressible fluids, *Commun. Pure Appl. Math.* 13 (2) (1960) 297–319.
- [8] E.E. Meshkov, Instability of the interface of two gases accelerated by a shock wave, *Fluid Dyn.* 4 (5) (1969) 101–104.
- [9] L. Rayleigh, Investigation of the character of the equilibrium of an incompressible heavy fluid of variable density, *Proc. Lond. Math. Soc.* 14 (1883) 170–177.
- [10] G. Taylor, The instability of liquid surfaces when accelerated in a direction perpendicular to their planes. Part 1. Waves on fluid sheets, *Proc. R. Soc. Lond. A Math., Phys. Sci.* 201 (1950) 192–196.
- [11] F. Marble, E. Zukoski, J. Jacobs, G. Hendricks, I. Waitz, Shock enhancement and control of hypersonic mixing and combustion, *AIAA 26th Joint Propulsion Conference* (1990).
- [12] E. Oran, J. Boris, *Numerical simulation of reactive flow*, Cambridge University Press, 2005.
- [13] M. Brouillette, The Richtmyer–Meshkov instability, *Annu. Rev. Fluid Mech.* 34 (2002) 445–468.
- [14] P.G. Drazin, *Introduction to hydrodynamic stability*, Cambridge University Press, 2002.
- [15] V.K. Tritschler, S. Hickel, X.Y. Hu, N.A. Adams, On the Kolmogorov inertial sub-range developing from Richtmyer–Meshkov instability, *Phys. Fluids* 25 (2013) 071701.
- [16] V.K. Tritschler, M. Zobel, S. Hickel, N.A. Adams, Evolution of length scales and statistics of Richtmyer–Meshkov instability from direct numerical simulations, *Phys. Rev. E* 90 (2014) 063001.
- [17] N.J. Zabusky, Vortex paradigm for accelerated inhomogeneous flows: visio-metrics for the Rayleigh–Taylor and Richtmyer–Meshkov environments, *Annu. Rev. Fluid Mech.* 31 (1999) 495–536.
- [18] J.-F. Haas, B. Sturtevant, Interaction of weak shock waves with cylindrical and spherical gas inhomogeneities, *J. Fluid Mech.* 181 (1987) 41–76.
- [19] J.J. Quirk, S. Karni, On the dynamics of a shock–bubble interaction, *J. Fluid Mech.* 318 (1996) 129–163.
- [20] M.A. Liberman, *Introduction to physics and chemistry of combustion: explosion, flame, detonation*, Springer, 2008.
- [21] W. Fickett, W.C. Davis, *Detonation: theory and experiment*, Dover Publications, 2010.
- [22] N.S. Haehn, D. Ranjan, C. Weber, J. Oakley, D. Rothamer, R. Bonazza, Reacting shock bubble interaction, *Combust. Flame* 159 (3) (2012) 1339–1350.
- [23] A.R. Miles, B. Blue, M.J. Edwards, J.A. Greenough, J.F. Hansen, H.F. Robey, R.P. Drake, C. Kuranz, D.R. Leibbrandt, Transition to turbulence and effect of initial conditions on three-dimensional compressible mixing in planar blast-wave-driven systems, *Phys. Plasmas* 12 (5) (2005) 056317.
- [24] A.W. Cook, Enthalpy diffusion in multicomponent flows, *Phys. Fluids* 21 (2009) 055109.
- [25] T. Poinsot, D. Veynante, *Theoretical and numerical combustion*, R T Edwards, 2001.
- [26] J. Troe, Predictive possibilities of unimolecular rate theory, *J. Phys. Chem.* 83 (1) (1979) 114–126.

- [27] M. Ó Conaire, H.J. Curran, J.M. Simmie, W.J. Pitz, C.K. Westbrook, A comprehensive modeling study of hydrogen oxidation, *Int. J. Chem. Kinet.* 36 (2004) 603–622.
- [28] N.S. Haehn, Experimental investigation of the reactive shock–bubble interaction, University of Wisconsin–Madison, 2012 Ph.D. thesis.
- [29] G. Strang, On the construction and comparison of difference schemes, *SIAM J. Numer. Anal.* 5 (3) (1968) 506–517.
- [30] S. Gottlieb, C.-W. Shu, Total variation diminishing Runge–Kutta schemes, *Math. Comput.* 67 (1998) 73–85.
- [31] P.L. Roe, Approximate Riemann solvers, parameter vectors, and difference schemes, *J. Comput. Phys.* 43 (1981) 357–372.
- [32] B. Larouturou, L. Fezoui, On the equations of multi-component perfect or real gas inviscid flow, *Lect. Notes Math.* 1402 (1989) 69–98.
- [33] X.Y. Hu, V.K. Tritschler, S. Pirozzoli, N.A. Adams, Dispersion–dissipation condition for finite difference schemes, *ArXiv e-prints* (2012) arXiv:1204.5088.
- [34] V.K. Tritschler, X.Y. Hu, S. Hickel, N.A. Adams, Numerical simulation of a Richtmyer–Meshkov instability with an adaptive central-upwind 6th-order WENO scheme, *Phys. Scr. T155* (2013) 014016.
- [35] R. Abgrall, S. Karni, Computations of compressible multifluids, *J. Comput. Phys.* 169 (2001) 594–623.
- [36] E. Johnsen, F. Ham, Preventing numerical errors generated by interface-capturing schemes in compressible multi-material flows, *J. Comput. Phys.* 231 (2012) 5705–5717.
- [37] V.K. Tritschler, A. Avdonin, S. Hickel, X.Y. Hu, N.A. Adams, Quantification of initial-data uncertainty on a shock-accelerated gas cylinder, *Phys. Fluids* 26 (2014) 026101.
- [38] V.K. Tritschler, B.J. Olson, S.K. Lele, S. Hickel, X.Y. Hu, N.A. Adams, On the Richtmyer–Meshkov instability evolving from a deterministic multimode planar interface, *J. Fluid Mech.* 755 (2014) 429–462.
- [39] P.N. Brown, G.D. Byrne, A.C. Hindmarsh, VODE: a variable-coefficient ODE solver, *SIAM J. Sci. Stat. Comput.* 10 (5) (1989) 1038–1051.
- [40] J.H. Niederhaus, J.A. Greenough, J.G. Oakley, D. Ranjan, M.H. Anderson, R. Bonazza, A computational parameter study for the three-dimensional shock–bubble interaction, *J. Fluid Mech.* 594 (2008) 85–124.
- [41] D. Ranjan, J.H.J. Niederhaus, J.G. Oakley, M.H. Anderson, J.A. Greenough, R. Bonazza, Experimental and numerical investigation of shock-induced distortion of a spherical gas inhomogeneity, *Phys. Scr. T132* (2008) 014020.
- [42] B. Hejazialhosseini, D. Rossinelli, P. Koumoutsakos, Vortex dynamics in 3D shock–bubble interaction, *Phys. Fluids* 25 (2013) 110816.
- [43] F. Nakamura, C.F. McKee, R.I. Klein, R.T. Fisher, On the hydrodynamic interaction of shock waves with interstellar clouds. II. The effect of smooth cloud boundaries on cloud destruction and cloud turbulence, *Astrophys. J. Suppl. Ser.* 164 (2) (2006) 477.
- [44] P.V. Danckwerts, The definition and measurement of some characteristics of mixtures, *Appl. Sci. Res. Sect. A* 3 (4) (1952) 279–296.
- [45] D. Ranjan, M. Anderson, J. Oakley, R. Bonazza, Experimental investigation of a strongly shocked gas bubble, *Phys. Rev. Lett.* 94 (2005) 184507.
- [46] R. Klein, K.S. Budil, T.S. Perry, D.R. Bach, The interaction of supernova remnants with interstellar clouds: experiments on the Nova laser, *Astrophys. J.* 583 (2003) 245–259.
- [47] S.E. Widnall, D.B. Bliss, C.-Y. Tsai, The instability of short waves on a vortex ring, *J. Fluid Mech.* 66 (1974) 35–47.
- [48] J. Giordano, Y. Burtschell, Richtmyer–Meshkov instability induced by shock–bubble interaction: numerical and analytical studies with experimental validation, *Phys. Fluids* 18 (3) (2006) 036102.
- [49] J.F. Hansen, H.F. Robey, R.I. Klein, A.R. Miles, Experiment on the mass-stripping of an interstellar cloud in a high Mach number post-shock flow, *Phys. Plasmas* 14 (5) (2007) 056505.
- [50] X. Wang, T. Si, X. Luo, J. Yang, Generation of Air/SF<sub>6</sub> interface with minimum surface feature by soap film technique, 29th International Symposium on Shock Waves 2, 2015, pp. 1065–1070.
- [51] L. Zou, S. Liao, C. Liu, Y. Wang, Z. Zhai, Aspect ratio effect on shock-accelerated elliptic gas cylinders, *Phys. Fluids* 28 (3) (2016) 036101.
- [52] P.Y. Georgievskiy, V.A. Levin, O.G. Sutyurin, Interaction of a shock with elliptical gas bubbles, *Shock Waves* 25 (4) (2015) 357–369.